ATLAS CONF Note

ATLAS-CONF-2019-026

11th July 2019

Inclusive and differential measurements of the charge asymmetry in $t\bar{t}$ events at 13 TeV with the ATLAS detector

The ATLAS Collaboration

A measurement of the top-antitop ($t\bar{t}$) charge asymmetry A_C is presented using data corresponding to an integrated luminosity of 139 fb^{-1} of $\sqrt{s}$ = 13 TeV of pp collisions recorded by the ATLAS experiment at the Large Hadron Collider, CERN. The measurement is performed in the single-lepton channel (e or μ) combining both the resolved and boosted topologies of top quark decays. A Bayesian unfolding procedure is used to infer the asymmetry at parton level, correcting for detector resolution and acceptance effects. The inclusive $t\bar{t}$ charge asymmetry is measured as $A_C = 0.0060 \pm 0.0015$(stat+syst.), which differs from zero by 4 standard deviations. Differential measurements are performed as a function of the invariant mass and longitudinal boost of the $t\bar{t}$ system. Both inclusive and differential measurements are found to be compatible with the Standard Model predictions, at NNLO in perturbation theory with NLO electroweak corrections.

1 Introduction

The large mass of the top quark, which is close to the electroweak symmetry breaking scale, indicates that this particle could play a special role in the Standard Model (SM) as well as in beyond the Standard Model (BSM) theories. Due to the high top-pair production ($t\bar{t}$) cross section for 13 TeVproton–proton (pp) collisions [1], the Large Hadron Collider (LHC) experiments collect an unprecedented number of events in which a $t\bar{t}$ pair is produced. The top quark has a very short lifetime ($\tau_t \approx 0.5 \times 10^{-24}$ s) and decays before hadronisation ($\tau^{\text{had}} \sim 10^{-23}$ s), therefore, several of its properties may be measured precisely from studies of the top quark's decay products. These measurements probe predictions of quantum chromodynamics (QCD), which provides the largest contribution to $t\bar{t}$ production. They also probe potential contributions from couplings between the top quark and BSM particles [2–4].

Production of top quark pairs is symmetric at leading-order (LO) under charge conjugation. The asymmetry between the t and $\bar{t}$ originates from interference of the higher-order amplitudes in the $q\bar{q}$ and qg initial states, with the $q\bar{q}$ annihilation contribution dominating. The contribution from electro-weak corrections is about 13% for the inclusive asymmetry and almost 20% for high $m_{t\bar{t}}$ bins [5–7] in the differential case. The $qg \to t\bar{t}g$ production process is also asymmetric, but its cross section is much smaller than $q\bar{q}$. Gluon fusion production is symmetric to all orders. As a consequence of these asymmetries, the top quark is preferentially produced in the direction of the incoming quark.

At a $p\bar{p}$ collider, where the preferential direction of the incoming quark (antiquark) always almost coincides with that of the proton (anti-proton), a forward-backward asymmetry A_{FB} can be measured directly [8–11]. At the LHC pp collider, since the colliding beams are symmetric, it is not possible to measure A_{FB} as there is no preferential direction of either the top quark or the top antiquark. However, due to the difference in the proton parton distribution functions, on average the valence quarks carry a larger fraction of the proton momentum than the sea antiquarks. This results in more forward top quarks and more central top antiquarks. A central–forward charge asymmetry for the $t\bar{t}$ production, referred to as the charge asymmetry (A_{C}) is defined as [8, 12, 13]:

$$A_C = \frac{N(\Delta|y| > 0) - N(\Delta|y| < 0)}{N(\Delta|y| > 0) + N(\Delta|y| < 0)}, \tag{1}$$

where $\Delta|y| = |y_t| - |y_{\bar{t}}|$ is the difference between the absolute value of the top-quark rapidity $|y_t|$ and the absolute value of the top-antiquark rapidity $|y_{\bar{t}}|$. At the LHC, the dominant $t\bar{t}$ production mechanism is via gluon fusion, especially for collisions with higher centre of mass energy. The contributions from $q\bar{q}$ and qg are small, so the charge symmetric $gg \to t\bar{t}$ process dilutes the measureable asymmetry.

Several BSM processes, such as anomalous vector or axial couplings (e.g. axigluons), heavy Z' bosons, or processes which interfere with the SM can alter A_{C} [2–4, 12, 14–21]. Several BSM models predict charge asymmetries which vary as a function of the invariant mass $m_{t\bar{t}}$ and the longitudinal boost of the $t\bar{t}$ system along the z-axis $\beta_{z,t\bar{t}}$.[1] In particular, BSM effects are expected to be enhanced in specific kinematic regions, for example, when the $\beta_{z,t\bar{t}}$ or $m_{t\bar{t}}$ are large [22]. Previously the CDF and D0 collaborations reported measurements of A_{FB} larger than the LO SM prediction [10, 11, 23–26], however these are in

[1] ATLAS uses a right-handed coordinate system with its origin at the nominal interaction point (IP) in the centre of the detector and the z-axis along the beam pipe. The x-axis points from the IP to the centre of the LHC ring, and the y-axis points upwards. Cylindrical coordinates (r, ϕ) are used in the transverse plane, ϕ being the azimuthal angle around the z-axis. The pseudorapidity is defined in terms of the polar angle θ as $\eta = -\ln\tan(\theta/2)$. Angular distance is measured in units of $\Delta R \equiv \sqrt{(\Delta\eta)^2 + (\Delta\phi)^2}$.

agreement with higher orders calculations. The measurements performed so far by both the ATLAS and CMS collaborations at $\sqrt{s}$=7, 8 and 13 TeV, in different decay channels and topologies, have demonstrated good agreement with SM predictions [27–37].

However, even for the combined ATLAS and CMS inclusive and differential measurements in lepton+jet channel at $\sqrt{s} = 7$ and $\sqrt{s} = 8$ TeV [38], uncertainties in kinematic regions such as high $m_{t\bar{t}}$ are statistically dominated and do not have the sensitivity to exclude BSM signals.

This document reports the measurement of A_C in $t\bar{t}$ production with 139 fb^{-1} of data at $\sqrt{s} = 13$ TeV recorded by the ATLAS experiment at the LHC. The measurement is made in $t\bar{t}$ events with a single isolated lepton in final state (lepton+jets), in both the resolved and boosted topologies of the top quark decays. The measurements in both topologies are combined and A_C is measured inclusively, as well as differentially as a function of the $m_{t\bar{t}}$ and $\beta_{z,t\bar{t}}$. A Bayesian unfolding procedure [39] is applied to correct for acceptance and detector effects, resulting in parton-level A_C measurements for comparison with theory calculations. This measurement exploits the large amount of data in two ways: reducing the statistical uncertainty and constraining the large uncertainties in-situ.

The document is organised as follows. The ATLAS detector is described in Section 2, and the object definitions and event selections are detailed in Sections 3 and 4, respectively. The signal and background modelling and the estimation of the fake lepton backgrounds are described in Section 5. The unfolding procedure is presented in Section 6. Section 7 discusses the systematics uncertainties, and the results are summarised in Section 8 with conclusions drawn in Section 9.

2 ATLAS detector

The ATLAS detector [40] covers nearly the entire solid angle around the collision point. It consists of an inner tracking detector (ID) surrounded by a thin superconducting solenoid, electromagnetic (EM) and hadronic calorimeters, and a muon spectrometer (MS), incorporating three large superconducting toroidal magnets. The ID is immersed in a 2 T axial magnetic field and provides charged-particle tracking in the range $|\eta| < 2.5$.

The high-granularity silicon pixel detector covers the proton collision region and typically provides four measurements per track. The first layer is the insertable B-layer (IBL), which was installed prior to 2015 data taking [41, 42]. Outside of this is the silicon microstrip tracker (SCT) which records up to eight measurements per track. These silicon detectors are complemented by the transition radiation tracker (TRT), which provides radially extended track reconstruction up to $|\eta| = 2.0$. The TRT also produces electron identification information based on the fraction of hits (typically 30 in total) above an energy-deposit threshold corresponding to transition radiation.

The calorimeter system covers the pseudorapidity range $|\eta| < 4.9$. Within the region $|\eta| < 3.2$, EM calorimetry is provided by high-granulairty barrel and endcap lead/liquid-argon (LAr) calorimeters, with an additional thin LAr presampler covering $|\eta| < 1.8$, to correct for energy loss in material upstream of the calorimeters. Hadronic calorimetry is provided by a steel/scintillating-tile calorimeter, which is segmented into three barrel structures within $|\eta| < 1.7$, and two copper/LAr hadronic endcap calorimeters. The solid angle coverage is completed with forward copper/LAr and tungsten/LAr calorimeter modules optimised for EM and hadronic measurements respectively.

The MS comprises separate trigger and high-precision tracking chambers. These measure the deflection of muons in a magnetic field generated by superconducting air-core toroids. The field integral of the toroids ranges between 2.0 and 6.0 T m across most of the detector. Tracking chambers cover the region $|\eta| < 2.7$ consisting of three layers of monitored drift tubes, which are complemented by cathode-strip chambers in the forward region where the background is highest. The muon trigger system covers the range $|\eta| < 2.4$ with resistive-plate chambers in the barrel, and thin-gap chambers in the endcap regions. Interesting events are selected to be recorded by the first-level (L1) trigger system using custom hardware. This is followed by selections made using algorithms implemented in software in the high-level trigger (HLT) [43]. The L1 trigger reduces the 40 MHz bunch crossing rate to below 100 kHz. The HLT further reduces this rate in order to record events to disk at 1 kHz.

3 Object definition and reconstruction

This analysis utilises reconstructed electrons, muons, jets, b-jets, large-radius (large-R) jets and missing transverse momentum.

The primary vertex (PV) of an event is that which has the highest $\sum p_{\mathrm{T}}^{\mathrm{track}}$ [44], where the sum extends over all associated tracks with $p_{\mathrm{T}} > 0.5$ GeV. At least two tracks are required.

Electron candidates are reconstructed from clusters in the EM calorimeter that are associated to tracks in the inner detector [45]. Candidates are required to have a transverse energy, E_{T}, greater than 28 GeV and $|\eta_{\mathrm{cluster}}| < 2.47$. If η_{cluster} is within the transition region between the barrel and the end-cap of the LAr calorimeter ($1.37 < |\eta_{\mathrm{cluster}}| < 1.52$) the electron candidate is removed. A multivariate algorithm is used to select signal electrons, which have to satisfy a "tight" likelihood-based quality criterion. Additional impact parameter criteria applied are $|d_0|/\sigma(d_0) < 5$ and $|z_0 \sin\theta| < 0.5$ mm. The electron candidates have to pass p_{T}- and η-dependent isolation requirements based on their tracks and clusters, which results in an electron reconstruction efficiency of 90% at $p_{\mathrm{T}} = 25$ GeV and 99% at $p_{\mathrm{T}} = 60$ GeV.

Muon candidates are reconstructed from ID tracks combined with track segments or full tracks in the MS [46]. Candidates are required to fulfill the "medium" identification quality criteria. Only muon candidates within $|\eta| < 2.5$, $p_{\mathrm{T}} > 28$ GeV, and with impact parameter criteria of $|d_0|/\sigma(d_0) < 3$ and $|z_0 \sin\theta| < 0.5$ mm, are selected. For muon candidates, the track isolation is defined similarly to electron candidates and the average identification efficiency is 98% as measured on data.

Jets are reconstructed with the anti-k_t algorithm [47] using a radius parameter $R = 0.4$ (small-R) from calibrated topological calorimeter clusters [48]. The jet calibration relies on Monte Carlo (MC) simulations, with additional corrections obtained using in-situ techniques to correct for differences observed between simulations and data. The jet energy is corrected for pile-up effects using a jet area method [49] and further corrected using a calibration based on both MC simulations as well as data [50]. Only jets with $p_{\mathrm{T}} > 25$ GeV and within the central region are selected. Additionally, a Jet Vertex Tagger (JVT) [51] is used to discriminate between jets originating from the PV and from pile-up collisions, for jets with $p_{\mathrm{T}} < 60$ GeV and $|\eta| < 2.4$. The selected JVT working point provides an average efficiency of 92% for hard-scatter jets and a rejection factor of 99% for pile-up jets.

Jets containing b-hadrons are identified ('b-tagged') using a multivariate algorithm. Inputs are combined from algorithms which use secondary vertices reconstructed within a jet and track impact parameters [52, 53]. For this measurement, the operating point corresponds to a 77% efficiency to tag b-quark jets, with a purity of 95%. The corresponding rejection factors for jets originating from a c-quark, light

quark or τ lepton are 5, 100, and 20, respectively. To account for possible mismodelling between data and predictions of the selection efficiencies for the different quark flavour jets and jets originating from hadronically-decaying τ leptons, per-jet scale factors are obtained from $t\bar{t}$ events in data [53, 54].

Large-R jets are reconstructed with the anti-k_t algorithm [47] from the individually-calibrated topological cell clusters [50, 55], using a radius parameter $R = 1.0$ and calibrated from simulation [56]. They are subsequently *trimmed* [57] to remove the effects of pile-up and underlying event. Trimming is a technique in which the original constituents of the jets are reclustered using the k_t algorithm [58] with a distance parameter R_{sub}, in order to produce a collection of sub-jets. Sub-jets with a fraction of the large-R jet p_{T} less than a calibrated threshold f_{cut} are removed. The trimming parameters used here are $R_{\text{sub}} = 0.2$ and $f_{\text{cut}} = 5\%$ based on previous studies [59]. The large-R jet moments (e.g. mass, τ_{32} [2]) are calculated using only the constituents of the selected sub-jets.

The missing transverse momentum [61], with magnitude $E_{\text{T}}^{\text{miss}}$, is calculated from a vectorial sum of all reconstructed objects. The calculation utilises calibrated electrons, muons, photons, hadronically decaying τ-leptons, and jets reconstructed from calorimeter energy deposits. These are combined with soft hadronic activity measured by reconstructed charged-particle tracks not associated to other hard objects.

In order to avoid double counting of the same energy clusters or tracks as different object types, an overlap removal procedure is applied. First, electron candidates sharing a track with any muon candidates are removed. Secondly, if the distance between a small-R jet and an electron candidate is $\Delta R < 0.2$, the jet is removed. If multiple small-R jets are found with this requirement, only the closest small-R jet is removed. If the distance between a small-R jet and an electron candidate is $0.2 < \Delta R < 0.4$, then the electron candidate is removed. If the distance between a small-R jet and any muon candidates is $\Delta R < 0.4$, the muon candidate is removed if the small-R jet has more than two associated tracks, otherwise the small-R jet is removed. Finally, if the distance between a large-R jet and the electron candidate is $\Delta R < 1.0$, the large-R jet is removed.

4 Event selection and reconstruction

The analysis uses data collected by the ATLAS detector between 2015 and 2018 from pp collisions at a centre-of-mass energy of $\sqrt{s} = 13$ TeV, corresponding to an integrated luminosity of 139 fb^{-1}. Only events recorded under stable beam conditions with all detector subsystems operational, with a primary vertex and passing a single-electron or single-muon trigger are considered. Multiple triggers are used to increase the selection efficiency. The lowest-threshold triggers utilise isolation requirements to reduce the trigger rate. These have p_{T} thresholds of 20 GeV for muons and 24 GeV for electrons in 2015 data, and 26 GeV for both lepton types in 2016, 2017 and 2018 data. They are complemented by other triggers with higher p_{T} thresholds and with no isolation requirements in order to increase event acceptance.

A common event selection is used for the resolved and boosted topologies, requiring exactly one lepton candidate matched to the trigger lepton with a minimum transverse momentum of 28 GeV. Events containing additional leptons with transverse momentum larger than 25 GeV are rejected. To reduce the impact of the multijet background, cuts on $E_{\text{T}}^{\text{miss}}$ and M_{T}^{W} are applied [3]. In the electron channel, both $E_{\text{T}}^{\text{miss}}$ and M_{T}^{W} are required to be larger than 30 GeV because of the higher level of multijet background (see

[2] the τ_{32} is defined in Ref. [60]

[3] $M_{\text{T}}^{W} = \sqrt{2p_{\text{T}}^{\ell}E_{\text{T}}^{\text{miss}}(1-\cos\Delta\phi)}$ where $\Delta\phi$ is the angle between the lepton and $E_{\text{T}}^{\text{miss}}$ in the transverse plane.

Sec. 5.4), while in the muon channel a triangular cut $E_{\mathrm{T}}^{\mathrm{miss}} + M_{\mathrm{T}}^{W} > 60$ GeV is applied. At least one of the small-R jets is required to be b-tagged. The selected events are further divided into 1b-tag-exclusive and 2b-tag-inclusive regions based on the b-jet multiplicity, while the electron and muon channels are summed.

4.1 Event selection and reconstruction in the resolved topology

The resolved topology requires at least four small-R jets with $p_{\mathrm{T}} > 25$ GeV. The $t\bar{t}$ system is reconstructed using a boosted decision tree (BDT) algorithm to find the correct assignment of the reconstructed final state objects to the $t\bar{t}$ decay products. Events which also pass the boosted selection are removed.

The challenge of reconstructing an event in the resolved topology is to correctly assign individual selected jets to the corresponding partons from the decaying top-quarks. For this purpose, an multivariate technique implemented within the `TMVA` package [62] is designed. The BDT combines kinematic event variables and b-tagging information, with weight information from the Kinematic Likelihood Fitter (KLFitter) [63], into a single discriminant. Each permutation of jet-to-parton assignments is evaluated and the permutation with the highest BDT score is used for the $t\bar{t}$ kinematic reconstruction.

Since the number of possible permutations rapidly increases with the jet multiplicity, only permutations of up to five jets are considered. If more than five jets are present in an event, the two highest b-tagging score jets are considered, together with the remaining three highest p_{T} jets. The $t\bar{t}$ signal sample (see Sec. 5.1) is used for the BDT training, while each jet-to-parton permutation is flagged as either "signal" or "background". Only permutations with four jets correctly assigned within $\Delta R = 0.3$ of the corresponding partons are flagged as signal, all other permutations are considered as combinatorial background. There is no attempt to correctly match the individual partons from the hadronically decaying W as it does not affect the reconstruction. The BDT aims to discriminate the signal from the combinatorial background and is trained separately for the 1b-exclusive and 2b-inclusive b-tag regions, but inclusively in the lepton flavour (electron, muon). The BDT is trained using only the background permutations with a significant probability of being mistakenly identified as signal, which are the ones for which the KLFitter calculates the highest likelihood.

Thirteen variables are used as input to the BDT:

- the reconstructed mass of the hadronically-decaying top quark,
- the logarithm of likelihood from the KLFitter,
- the reconstructed mass of the hadronically-decaying W boson,
- b-tagging information for the b-jet from the semileptonically-decaying top quark,
- the b-jet from the hadronically-decaying top quark,
- the light-jet from the W boson decay,
- the reconstructed mass of the semileptonically-decaying top quark,
- the ΔR between b-jet from semileptonically-decaying top quark and lepton,
- the ΔR between the two light jets from W decay,
- the p_{T} of the lepton and b-jet from semileptonically-decaying top quark,

- the number of jets in the event,
- the pseudorapidity of the hadronically-decaying top quark,
- and finally the ΔR between the two b-jets from $t\bar{t}$ decay.

For the final selection, events are required to have a BDT discriminant for the best permutation with a score > 0.3 in order to reject $t\bar{t}$ combinatorial backgrounds and suppress non-$t\bar{t}$ background processes as they naturally populate low regions of BDT since no permutation matches expected kinematics of $t\bar{t}$. Using the lower threshold on the BDT discriminant increases the signal to non-$t\bar{t}$ background ratio by a factor of ~ 2. In addition, for $t\bar{t}$ signal events where a jet-to-parton assignment is possible for all partons from $t\bar{t}$ decay, the correct assignment is found for 75% of the events.

4.2 Event selection and reconstruction in the boosted topology

In the boosted topology, the reconstruction aims to identify one high p_{T} and collimated hadronic top-quark decay and at least one small-R jet with $p_{\mathrm{T}} > 25$ GeV close to the selected lepton with $\Delta R(\mathrm{jet}_{R=0.4}, \ell) < 1.5$. If multiple small-$R$ jets satisfy this condition, the one with highest p_{T} is considered for the subsequent boosted top quark reconstruction. In addition, at least one large-R top-tagged jet with $p_{\mathrm{T}} > 350$ GeV and $|\eta| < 2$ is required as the hadronically-decaying top quark. Since both top quarks are expected to be back-to-back in the $t\bar{t}$ rest frame, additional cuts related to the large-R jet, the isolated lepton and the small-R jet close to the lepton are applied: $\Delta\phi(\mathrm{jet}_{R=1.0}, \ell) > 2.3$ and $\Delta R(\mathrm{jet}_{R=1.0}, \mathrm{jet}_{R=0.4}) > 1.5$. The large-$R$ jet is evaluated by a top-tagging algorithm utilising jet mass and τ_{32} substructure [60] variables, where an operating point with an efficiency of 80% is chosen. The top tagger is optimised using the same approach as described in Ref. [64]. Finally, a cut on the invariant mass of the reconstructed $t\bar{t}$ system of $m_{t\bar{t}} > 500$ GeV is applied. This criterion is imposed to remove a negligible fraction (0.1%) of poorly-reconstructed events which pass the boosted selection criteria above. In addition, this removes the lowest $m_{t\bar{t}}$ bin in the corresponding differential A_{C} measurement which would suffer from extremely low statistics.

The four-momentum of the leading-p_{T} large-R jet satisfying the selection criteria is taken as the four-momentum estimate of the hadronically-decaying top quark. The semileptonically-decaying top-quark four-momentum is constructed from the isolated lepton, the selected small-R jet and the neutrino four-momentum. The neutrino four-momentum is calculated using the constraints from the $E_{\mathrm{T}}^{\mathrm{miss}}$ value, the lepton kinematics and the W boson mass. If there are two possible solutions for the neutrino four-momentum, the solution with the minimum $|p_z|$ is chosen. If there is no real solution, the $E_{\mathrm{T}}^{\mathrm{miss}}$ vector is varied in the transverse plane by the minimum amount necessary to obtain at least one solution.

5 Signal and background modelling

All signal and background processes are modelled using MC simulations, with the exception of non-prompt lepton and non-leptonic particle (fake lepton) backgrounds, which are estimated from data (see Sec. 5.4). All simulated samples use EvtGen v1.6.0 [65] to model the decays of heavy hadrons, with the exception of the background samples generated with Sherpa [66]. Most of the MC samples are processed using a full simulation of the detector response with the GEANT4 toolkit [67]. The samples used to estimate modelling systematic uncertainties are either obtained by reweighing the default full simulation samples, or

are produced using fast simulation software ATLFASTII [68]. To model additional pp interactions from the same or neighbouring bunch crossings, the hard scattering events are overlaid with a set of minimum-bias interactions generated using Pythia8 [69] and the MSTW2008LO [70] parton distribution function (PDF) set with the A3 [71] tuned parameter settings. Finally, the simulated MC events are reconstructed using the same software as the data. Detailed explanations on the MC samples for the signal and for each background are provided in the following.

5.1 $t\bar{t}$ signal

All $t\bar{t}$ samples, except for mass variation samples, assume a top-quark mass of $m_{\text{top}} = 172.5$ GeV and are normalised to the inclusive production cross section of $\sigma(t\bar{t}) = 832 \pm 51$ pb. This cross section is calculated at next-to-next-to-leading order (NNLO) in QCD including the resummation of next-to-next-to-leading logarithm (NNLL) soft-gluon terms using Top++2.0 [72–78]. The uncertainties on the cross-section due to PDF and α_s are calculated using the PDF4LHC prescription [79] with the MSTW2008 68% CL NNLO [70, 80], CT10 NNLO [81, 82] and NNPDF2.3 5f FFN [83] PDF sets, and are added in quadrature to the scale uncertainty.

The nominal $t\bar{t}$ events are generated with the PowhegBox [84–87] v2 generator which provides matrix elements at next-to-leading order (NLO) in the strong coupling constant α_S, with the NNPDF3.0NLO [88] PDF and the h_{damp} parameter[4] set to 1.5 m_{top} [89]. The functional form of the renormalisation and factorisation scales (μ_r and μ_f) is set to the nominal scale of $\sqrt{m_{\text{top}}^2 + p_{\text{T}}^2}$. The events are interfaced with Pythia8.230 for the PS and hadronisation, using the A14 set of tuned parameters [90] and the NNPDF23LO PDF set.

To study the $t\bar{t}$ modelling uncertainties, alternative samples which use the ATLFASTII simulation are considered.

The uncertainty due to initial-state-radiation (ISR) is estimated from an altered $t\bar{t}$ sample with variations in the additional radiation [91]. To simulate higher parton radiation, μ_r and μ_f are varied by a factor of 0.5 while simultaneously increasing the h_{damp} value to 3 m_{top}. The nominal $t\bar{t}$ signal sample is used to estimate reduced initial-state radiation, by varying the scales by a factor of 2.0 using weights. The impact of final-state-radiation (FSR) is evaluated using PS weights in Pythia8, for the up and down variations the renormalisation scale for QCD emission in FSR is altered factors of 0.5 and 2.0, respectively.

The impact of the PS and hadronisation model is evaluated using the nominal generator, but interfaced with Herwig7.04 [92, 93] using the H7UE set of tuned parameters [93], and the MMHT2014LO PDF set [94].

To assess the uncertainty due to the choice of the matching scheme MadGraph5_aMC@NLO (referred to as MG5_aMC in the following) [95] and Pythia8 is used. The calculation of the hard-scattering uses MG5_aMC v2.6.0 with the NNPDF3.0NLO [88] PDF set. Events are interfaced with Pythia8.230 [69], using the A14 set of tuned parameters [90] and the NNPDF23LO PDF. The shower starting scale has the functional form $\mu_q = H_T/2$ [91], where H_T is defined as the scalar sum of the p_T of all outgoing partons. The renormalisation and factorisation scale choice is the same as used with Powheg .

[4] The h_{damp} parameter controls the transverse momentum p_T of the first additional emission beyond the LO Feynman diagram in the parton shower (PS) and therefore regulates the high-p_T emission against which the $t\bar{t}$ system recoils.

To study the effect on A_C of different values of the top-quark mass, two samples are generated using the same settings as in the nominal $t\bar{t}$ signal sample (POWHEG + PYTHIA8), but with m_{top} set to either 172 GeV or 173 GeV.

Finally, the PROTOS generator [96] with the CTEQ6L1 PDF set is used to generate $t\bar{t}$ samples predicting different asymmetry values due to the inclusion of a new heavy axigluon. The generated samples contain only parton level information, which is later used to re-weight the nominal $t\bar{t}$ POWHEG +PYTHIA8 sample.

5.2 Single top

Single-top tW associated production is modelled using the POWHEGBOX [85–87, 97] v2 generator which provides matrix elements at NLO in α_S, using the five flavour scheme with the NNPDF3.0NLO [88] PDF set. The functional form of μ_r and μ_f is set to the nominal scale of $\sqrt{m_{\text{top}}^2 + p_T^2}$. The diagram removal scheme [98] is employed to treat the interference with $t\bar{t}$ production [89]. Dedicated samples with a diagram subtraction (DS) scheme [98] are considered to evaluate the uncertainty due to the treatment of the overlap with $t\bar{t}$ production.

Single-top t-channel (s-channel) production is modelled using the POWHEGBOX [85–87, 99, 100] v2 generator which provides matrix elements at NLO in α_S , using the four (five) flavour scheme with the NNPDF3.0NLO [88] PDF set. The functional form of μ_r and μ_f is set to $\sqrt{m_b^2 + p_{T,b}^2}$ [99].

For these processes, the events are interfaced with PYTHIA8.230 [69] using the A14 tune [90] and the NNPDF23LO PDF set.

The uncertainty due to ISR is estimated using varied weights in the matrix element (ME) and in the PS. To simulate higher ISR, μ_r and μ_f are varied by a factor of 0.5 in the ME. For the simulation of lower ISR, μ_r and μ_f are varied by a factor of 2.0. The impact of increased or decreased FSR is evaluated using PS weights, which vary the renormalisation scale for QCD emission in the FSR by a factor of 0.5 and 2.0, respectively.

The impact of the PS and hadronisation model is evaluated by comparing the nominal generator sample with events produced with the POWHEGBOX [85–87, 97] v2 generator at NLO in QCD. These use the five (four) flavour scheme for tW and s-channel (t-channel) process(es), and the NNPDF3.0NLO [88] PDF set. The events are interfaced with HERWIG7.04 [92, 93], using the H7UE set of tuned parameters [93] and the MMHT2014LO PDF set [94].

To assess the uncertainty due to the choice of the matching scheme, the nominal sample is compared to a sample generated with the MG5_AMC v2.6.2 generator at NLO in QCD in the five (four) flavour scheme for tW and s-channel (t-channel) process(es), using the NNPDF3.0NLO [88] PDF set. The events are interfaced with PYTHIA8.230 [69], using the A14 set of tuned parameters [90] and the NNPDF23LO PDF.

5.3 W and Z bosons with additional jets

QCD V+jets production is simulated with the SHERPA v2.2.1 [66] PS MC generator. In this setup, NLO matrix elements for up to two jets, and LO matrix elements for up to four jets are calculated with the Comix [101] and OpenLoops [102, 103] libraries. The nominal SHERPA PS [104], based on Catani-Seymour

dipoles and the cluster hadronisation model [105], are used, which employ a dedicated set of tuned parameters developed by the SHERPA authors based on the NNPDF3.0NNLO PDF set [88]. The V+jets samples are normalised to a NNLO prediction [106].

5.4 Non-prompt and fake leptons background

Non-prompt and fake lepton events, referred from here on as multijet events, can enter the selected data samples if a non-prompt or fake lepton is reconstructed. Several production mechanisms or mistakes in event reconstruction can produce such leptons. These includes semileptonic decays of heavy flavour hadrons, long-lived weakly decaying states (e.g. $\pi^{\pm}$, K mesons), π^0 mesons mis-reconstructed as electrons, electrons from photon conversions, or direct photons. To estimate the total contribution of multijet events a data-driven 'matrix-method' [107] is used. Two categories of events are selected, satisfying "loose" (identification only) and "tight" (identification and isolation) lepton selection requirements. The real (fake) lepton efficiency, ϵ_{real} (ϵ_{fake}), is defined as the ratio of the number of events with real (non-prompt/fake) lepton satisfying the tight selection to the number of events with real (non-prompt/fake) lepton satisfying the loose selection. The real lepton efficiency is measured in data using a tag-and-probe method on Z decays with two leptons and jets in the final state, while the fake efficiency is measured in control regions enriched in fake/non-prompt leptons. The sample of multijet events is estimated by the weighted data events, where the weight depends on the real and fake lepton efficiencies.

5.5 Other backgrounds

Diboson (VV) samples are simulated with the SHERPA v2.2.1 and v2.2.2 [66] PS MC generator. SHERPA v2.2.2 is used for two- and three-lepton samples. Additional hard parton emissions [101] are matched to a PS based on Catani-Seymour dipoles [104], using a dedicated set of tuned parton-shower parameters developed by the SHERPA authors, and the NNPDF3.0NNLO PDF set [88]. Matrix element and PS matching [108] is employed for different jet multiplicities which are then merged into an inclusive sample using using an improved CKKW matching procedure [109, 110]. The procedure is extended to NLO using the MEPS@NLO prescription [111]. These simulations are at NLO for up to one additional parton and at LO for up to three additional parton emissions using factorised on-shell decays. The virtual QCD corrections for matrix elements at NLO are provided by the OpenLoops library [102, 103]. The calculation is performed in the G_μ scheme, ensuring an optimal description of pure electroweak interactions at the electroweak scale.

The production of $t\bar{t}V$ and $t\bar{t}H$ events is modelled using the MG5_aMC v2.3.3 and POWHEGBOX [84–87] generators, respectively. The generators provide matrix elements at NLO in α_S, with the NNPDF3.0NLO [88] PDF set. Exceptionally, the production of $t\bar{t}H$ events corresponding to data collected in 2018 is modelled using the MG5_aMC v2.6.0 generator. For $t\bar{t}V$ and $t\bar{t}H$ production, the events are interfaced with PYTHIA8.210 [69] and PYTHIA8.230 [69], respectively. Each uses the A14 set of tuned parameters [90] and the NNPDF23LO [88] PDF set.

6 Unfolding

The $\Delta|y|$ distributions, used to extract A_{C}, are smeared by acceptance and detector resolution effects. The estimation of the true $\Delta|y|$, defined in MC using the t and $\bar{t}$ after final state radiation but before decay, is estimated from data using an unfolding procedure. The fully Bayesian unfolding (FBU) [39] method is used to unfold the observed data. FBU is an application of Bayesian inference to the unfolding problem. Given the observed data $\boldsymbol{D}$, and a response matrix $\mathcal{M}$ which models the detector response to a true distribution $\boldsymbol{T}$, the posterior probability of the true distribution follows the probability density:

$$p\left(\boldsymbol{T}|\boldsymbol{D},\mathcal{M}\right) \propto \mathcal{L}\left(\boldsymbol{D}|\boldsymbol{T},\mathcal{M}\right)\cdot\pi\left(\boldsymbol{T}\right), \tag{2}$$

where $p\left(\boldsymbol{T}|\boldsymbol{D},\mathcal{M}\right)$ is the posterior probability of the true distribution $\boldsymbol{T}$ under the condition of $\boldsymbol{D}$ and $\mathcal{M}$, $\mathcal{L}\left(\boldsymbol{D}|\boldsymbol{T},\mathcal{M}\right)$ is the likelihood function of $\boldsymbol{D}$ for a given $\boldsymbol{T}$ and $\mathcal{M}$, and $\pi\left(\boldsymbol{T}\right)$ is the prior probability density for the true distribution $\boldsymbol{T}$.

For this measurement, in all bins a uniform prior probability density is chosen for $\pi\left(\boldsymbol{T}\right)$, such that equal probabilities to all $\boldsymbol{T}$ spectra within a wide range are assigned. The response matrix is estimated from the simulated sample of $t\bar{t}$ events and the unfolded asymmetry A_{C} is computed from $p\left(\boldsymbol{T}|\boldsymbol{D},\mathcal{M}\right)$ as:

$$p\left(A_{\mathrm{C}}|\boldsymbol{D}\right) = \int \delta(A_{\mathrm{C}} - A_{\mathrm{C}}(\boldsymbol{T}))p\left(\boldsymbol{T}|\boldsymbol{D},\mathcal{M}\right)d\boldsymbol{T}. \tag{3}$$

The treatment of systematic uncertainties is naturally included in the Bayesian inference approach by extending the likelihood $\mathcal{L}\left(\boldsymbol{D}|\boldsymbol{T}\right)$ to include nuisance parameters. The marginal likelihood is defined as:

$$\mathcal{L}\left(\boldsymbol{D}|\boldsymbol{T}\right) = \int \mathcal{L}\left(\boldsymbol{D}|\boldsymbol{T},\boldsymbol{\theta}\right)\cdot\mathcal{N}(\boldsymbol{\theta})\,d\boldsymbol{\theta}, \tag{4}$$

where $\boldsymbol{\theta}$ are the nuisance parameters, and $\mathcal{N}(\boldsymbol{\theta})$ are their prior probability densities. These are assumed to be Gaussian distributions G with $\mu = 0$ and $\sigma = 1$. One nuisance parameter is associated with each of the uncertainty sources.

In FBU, the marginalisation approach provides a framework to treat simultaneously the unfolding and the background estimations using multiple data regions. Given the data distribution $\boldsymbol{D}_i$ measured in N_{ch} independent channels, the likelihood can be extended to a product of likelihoods in each channel as:

$$\mathcal{L}\left(\{\boldsymbol{D}_1\cdots\boldsymbol{D}_{N_{ch}}\}|\boldsymbol{T}\right) = \int \prod_{i=1}^{N_{ch}} \mathcal{L}\left(\boldsymbol{D}_i|\boldsymbol{T};\boldsymbol{\theta}\right)\cdot\mathcal{N}(\boldsymbol{\theta})\,d\boldsymbol{\theta}, \tag{5}$$

where the nuisance parameters are common to all analysis channels. The likelihood is sampled around its minimum using Markov-Chain Monte Carlo-based method in order to estimate the posterior probability of all the parameters of interest. In this measurement, the events are divided into four independent channels according event topology (resolved, boosted) and b-tag multiplicity (1-b exclusive, 2-b inclusive).

7 Systematic uncertainties

The inclusive and differential measurements are affected by several sources of systematic uncertainties, including signal and background modelling, experimental uncertainties, uncertainty on the response matrix due to limited MC statistics, and uncertainties due to unfolding. The individual systematic uncertainty sources are described in this section. Systematic uncertainties described in Sections 7.1 – 7.2 are symmetrised by taking half of the difference between the up and the down variation.

7.1 Experimental uncertainties

Luminosity: The uncertainty in the combined 2015–2018 integrated luminosity is 1.7% [112], obtained using the LUCID-2 detector [113] for the primary luminosity measurements.

Pile-up: The uncertainty on the reweighting procedure used to correct the pile-up profile in MC to match the data, is based on the disagreement between the instantaneous luminosity in data [114] and in simulation.

Lepton identification, reconstruction, isolation and trigger: The uncertainties are obtained with data using a tag-and-probe method on events with Z boson, W boson, and J/ψ decays [45, 115].

Lepton momentum scale and resolution: The uncertainties are evaluated using studies with reconstructed distributions of $Z \to \ell^+\ell^-$, $J/\psi \to \ell\ell$ and $W \to e\nu$ using methods similar to those in Refs. [115, 116].

Jet vertex tagger efficiency: This includes the uncertainty on the estimation of the residual contamination from pile-up jets after pile-up suppression, and a systematic uncertainty assessed by using different MC generators for simulation of $Z \to \mu\mu$ and $t\bar{t}$ events [117].

Jet energy scale: The uncertainty is assessed in data [50], using MC-based corrections and in situ techniques. It is broken down into a set of 29 decorrelated nuisance parameters, with contributions from pile-up, jet flavour composition, single-particle response, and punch-through. The parameters each have different jet p_{T} and η dependencies [118].

Jet energy resolution: The uncertainty is determined by an eigenvector decomposition strategy similar to the jet energy scale systematic uncertainties. Eight nuisance parameters take into account various effects evaluated from simulation-to-data comparisons. The magnitude of the jet energy resolution (JER) uncertainty variation is parametrised in jet p_{T} and η [118].

Large jet moment scale and resolution: The scale of the detector response for all relevant jet moments (p_{T}, m_{jet}, τ_{32}) is derived by comparing the calorimeter response to the tracker response for a matched reference track jet [59]. The resolution of the detector response is conservatively estimated as a 2% absolute uncertainty on p_{T} and 20% relative uncertainty on jet mass (where the nominal resolution to be smeared is parametrised in jet p_{T} and $m_{\mathrm{jet}}/p_{\mathrm{T}}$) [119]. A set of 14 nuisance parameters is used to estimate uncertainties due to these effects.

Flavour tagging: The uncertainties related to the b-jet tagging calibration are determined separately for b-jets, c-jets and light-jets, and comprise of nine, four and four eigenvector variations to the tagging efficencies, respectively [53, 54, 120]. In addition, two variations are assigned to the high-p_{T} extrapolation of both the b-jet and c-jet efficiencies, respectively.

Missing transverse energy scale and resolution: Different uncertainty sources are combined into two nuisance parameters for the total uncertainty on the scale and resolution of $E_{\mathrm{T}}^{\mathrm{miss}}$ [61].

7.2 Signal modelling

During the unfolding procedure, the $t\bar{t}$ signal normalisation is a free parameter in all the bins of the true $\Delta|y|$ distribution, and its posterior probability is being estimated. Therefore, the overall normalisation effect (affecting all $\Delta|y|$ bins simultaneously) of each signal modelling uncertainty that compare two specific generator configurations is removed. Only the shape difference affecting the $\Delta|y|$ bins separately is considered. In addition, these uncertainties are considered to be uncorrelated between the resolved and boosted regions, as the kinematics of the events are significantly different.

Matching uncertainty, parton shower and hadronisation modelling: To evaluate the uncertainty due to the choice of the matching scheme the $t\bar{t}$ PowhegBox + Pythia8 (nominal) sample is compared to the MG5_aMC + Pythia8 sample. Similarly, the uncertainty arising from the choice of PS, underlying event, and the hadronisation model is estimated from a comparison of the alternative PowhegBox + Herwig7 sample and the nominal $t\bar{t}$ signal sample.

Radiation modelling: The uncertainty arising from ISR is obtained using PS weights to vary the factorisation and renormalisarion scales by a factor of 2.0 for reduced radiation, and by using an alternative PowhegBox + Pythia8 sample (with the scales varied by a factor of 0.5 and with the h_{damp} parameter increased to 3 m_{top}) for enhanced radiation. The uncertainty arising from FSR is obtained using PS weights to vary the renormalisation scale by a factor of 2.0 or 0.5 for reduced or enhanced radiation, respectively.

Parton distribution functions: The uncertainty is obtained using the PDF4LHC15 prescription [121], which utilises a set of 30 separate nuisance parameters.

Top-quark mass variations: To estimate the effect of the uncertainty on the value of the top-quark mass, two samples are generated using PowhegBox v2 interfaced with Pythia8.230, with m_{top} set to either 172 GeV or 173 GeV. The A_{C} variations are calculated with respect to the nominal $t\bar{t}$ signal sample of 172.5 GeV . Only the variation that yields the larger uncertainty difference is considered for the final unfolding.

7.3 Background modelling

***W* + jets:** This charge asymmetric process is the dominant background in the 1b-exclusive region. Variations on W + jets [122] production which alter its predicted shape are used to estimate a modelling uncertainty. By reweighting the nominal W + jets prediction using dedicated MC generator weights, variations are considered on the renormalisation and factorisation scales, matrix-element-to-parton-shower matching CKKW scale [109, 123], and the scale used for the resummation of soft gluon emission. The shape and normalisation effects obtained from the scale variations are treated separately. The normalisation uncertainty is estimated to be $\sim$ 26% (53%) for 1-b exclusive (2-b inclusive) regions. In addition, a cross section uncertainty of 5% [124] is included.

Single-top: Single-top production is non-negligible in particular in the 2b-inclusive region. As the main contribution comes from the tW channel, an uncertainty of 5.3% [125, 126] is assigned to the predicted cross-section. In addition, the MC samples used for $t\bar{t}$ and single-top tW production contain an overlap in the final state. This is removed by the *diagram removal* (DR) scheme [97]. An alternative

approach of *diagram subtraction* (DS) [97] can also be used. To estimate the uncertainty, the difference between the nominal single-top prediction with DR and a single-top prediction with tW using DS is considered. Furthermore, uncertainties due to matching scheme, PS and hadronisation, and initial- and final-state radiation are taken into account. The matching scheme uncertainty is estimated by comparing the PowhegBox + Pythia8 (nominal single-top) samples with MG5_aMC + Pythia8 samples. The PS and hadronisation uncertainty is evaluated by comparing the nominal sample with a sample produced with PowhegBox and interfaced with Herwig7.04. The uncertainties arising from ISR and FSR are obtained by varying the scales by factors of 0.5 and 2.0, using the PS weights from the nominal single-top samples.

Multijet: In the matrix method, the real and fake lepton efficiencies are parametrised. To estimate the shape uncertainty, an alternative parametrisation of real and fake lepton efficiencies are compared to the nominal parametrisation, in each region. In addition, a 50% normalisation uncertainty is considered.

Other physics backgrounds: Other physics backgrounds with small contributions include Z + jets, diboson, $t\bar{t}V$, and $t\bar{t}H$ production. They are treated as a single background process in the unfolding procedure, and a cross-section normalisation uncertainty of 50% is applied.

7.4 Method uncertainties

Uncertainty on the response matrix due to limited MC statistics: Given the limited MC statistics of the $t\bar{t}$ signal sample, the bins of the response matrix are estimated with limited statistical precision. To estimate the resulting uncertainty on A_C, the Asimov unfolding is repeated multiple times with smeared response matrices (according to the MC statistics) to obtain a distribution of pseudoexperiment results for A_C. The width of this distribution is considered as the uncertainty, which is then summed in quadrature with the total uncertainty obtained from the unfolding. The bins of the response matrix are smeared according to Poisson statistics, according to the number of events in each bin.

Unfolding bias: The response of the unfolding procedure is determined from eight pseudo-datasets generated with PROTOS, each composed of the nominal $t\bar{t}$ signal reweighted to simulate a specific asymmetry. The injected A_C values range between -0.05 and 0.06, depending on the differential variable and bin. By unfolding the eight reweighted pseudo-datasets with the nominal response matrix, including all systematics uncertainties, the uncertainty associated to the unfolding response is calculated as: $A_C^{\text{meas}} - (A_C^{\text{meas}} - b)/a$, where a and b are the slope and offset of a linear fit of the generator-level (intrinsic) A_C to the unfolded A_C of the eight reweighted pseudo-datasets, and A_C^{meas} is the measured asymmetry value in data. In Tab. 2 this uncertainty is referred to as "Bias".

8 Results

8.1 Measurement

The event yields after the event selection can be found in Table 1.

Process:	Resolved		Boosted	
	1b-excl.	2b-incl.	1b-excl	2b-incl.
$t\bar{t}$	1520000±120000	1840000±150000	50000± 7000	74000±10000
Single top	89000± 12000	49000± 8000	3600± 1200	3000± 1200
W + jets	200000± 23000	23000± 14000	10000± 5000	1800± 1000
$Z + VV + t\bar{t}X$	52000± 28000	15000± 8000	2600± 1300	1400± 800
Multijet	90000± 40000	47000± 23000	3000± 1500	2300± 1200
Total Prediction	1950000±200000	1980000±160000	69000±11000	83000±11000
Data (139 fb^{-1})	1945037	2009526	54710	66582

Table 1: Event yields split by topology (resolved, boosted) and b-tag multiplicity (1-excl., 2-incl.). Total pre-marginalisation uncertainty is shown.

The measurement of A_C, which is inferred from $\Delta|y|$ following Equation 1, is performed using a fit that maximises the extended likelihood of Equation 5. A combination of four channels based on the b-jet multiplicity and the event topology (resolved or boosted) is employed. The $\Delta|y|$ distribution is split into four bins in all channels and in each differential bin of all differential measurements. Furthermore, since many BSM theories predict enhancement of the asymmetry at large $m_{t\bar{t}}$ and $\beta_{z,t\bar{t}}$ the differential bins have been chosen based on a compromise between data statistics and event migration due to bad reconstruction. A normalisation difference between the data and the predictions on the order of 20% is observed in the boosted channel and can be seen on Figures 1 – 3. This overestimation of the MC predictions at large values of top p_T (>300 GeV), is confirmed by differential cross-sections measurements [127]. In order to compensate for this known mismodeling, an additional free normalisation parameter K_{boosted} described by a uniform prior in the range 0-2, is added in the boosted channel. The posterior probability density is:

$$p\left(\boldsymbol{T}|\{\boldsymbol{D}_1 \cdots \boldsymbol{D}_{N_{ch}}\}\right) = \int \prod_{i=1}^{N_{ch}} \mathcal{L}\left(\boldsymbol{D}_i|\boldsymbol{R}_i(\boldsymbol{T}, K_{\text{boosted}}; \boldsymbol{\theta}_s), \boldsymbol{B}_i(\boldsymbol{\theta}_s, \boldsymbol{\theta}_b)\right) \mathcal{N}(\boldsymbol{\theta}_s)\, \mathcal{N}(\boldsymbol{\theta}_b)\, \pi(\boldsymbol{T})\, \pi(K_{\text{boosted}})\, \mathrm{d}\boldsymbol{\theta}_s\, \mathrm{d}\boldsymbol{\theta}_b, \tag{6}$$

where $\boldsymbol{B} = \boldsymbol{B}(\boldsymbol{\theta}_s, \boldsymbol{\theta}_b)$ is the total background prediction, the probability densities π are uniform priors and $\boldsymbol{R}$ is the reconstructed signal prediction. Two categories of nuisance parameters are considered: the normalisation of the background processes ($\boldsymbol{\theta}_b$), and the uncertainties associated with object identification, reconstruction and calibrations ($\boldsymbol{\theta}_s$). The latter uncertainties are referred to as detector systematic uncertainties, and affect both the reconstructed distribution of the $t\bar{t}$ signal and the total background prediction. The additonal boosted $t\bar{t}$ normalisation factors are found to be ~ 0.8 with a relative uncertainty between 7 and 15% depending on the measurement.

A Bootstrap [128] method is applied in order to estimate the effect on the systematic uncertainties of limited MC statistics in the alternative samples. Only systematic variations which are found to be significant compared to their statistical precision are kept. When systematic effects are found not to be significant, the respective uncertainty is set to 0.

In addition, a pruning procedure is implemented in order to remove the smallest systematic uncertainties and to simplify the marginalisation procedure. Since the A_C value is affected more by the shape effects of

the systematic uncertainties than by the normalisation effects, different pruning criteria are used to ignore the shape or normalisation effect of each systematic uncertainty.

As shown on Figures 1 – 3, the marginalisation procedure reduces the total uncertainty significantly and improves the agreement between the data and the predictions.

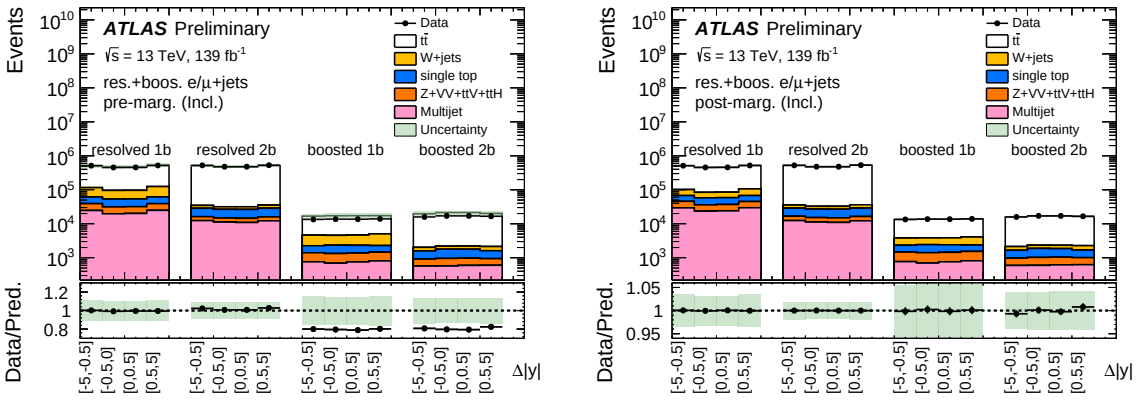

(a) (b)

Figure 1: Comparison between the data and the prediction for bins used in the inclusive A_C measurements in the lepton+jets channel. This comparison is shown before (left) and after (right) marginalisation within FBU. The bottom panels show the ratio of data to the predictions. The light green bands correspond to the total uncertainty of the prediction.

In order to determine the relative impact of each systematic uncertainty, pseudo-datsets are produced by shifting each systematics individually. These distributions are unfolded, and the difference between the resulting A_C values and the nominal unfolded A_C value is used to rank each systematic's impact.

The results of the unfolded data are summarised in Table 2. The ranking of the leading systematic uncertainties and the posterior probability distribution of A_C for the inclusive measurement are shown in Fig. 4.

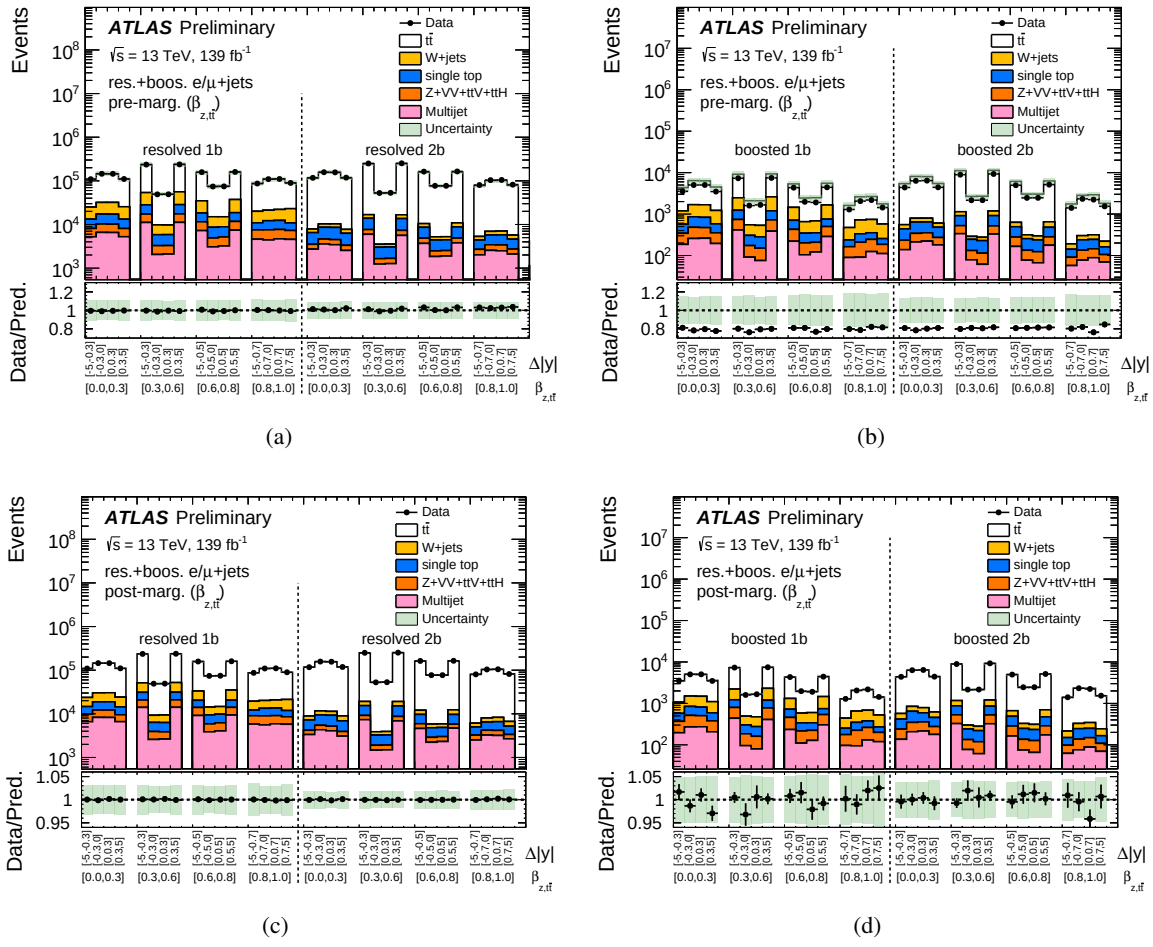

Figure 2: Comparison between the data and the prediction for bins used in the $\beta_{z,t\bar{t}}$ differential A_C measurements in the lepton+jets channel. This comparison is shown before (upper) and after (lower) marginalisation within FBU for resolved (left) and boosted (right) topology. The bottom panels show the ratio of data to the prediction. The light green bands correspond to the total uncertainty of the prediction.

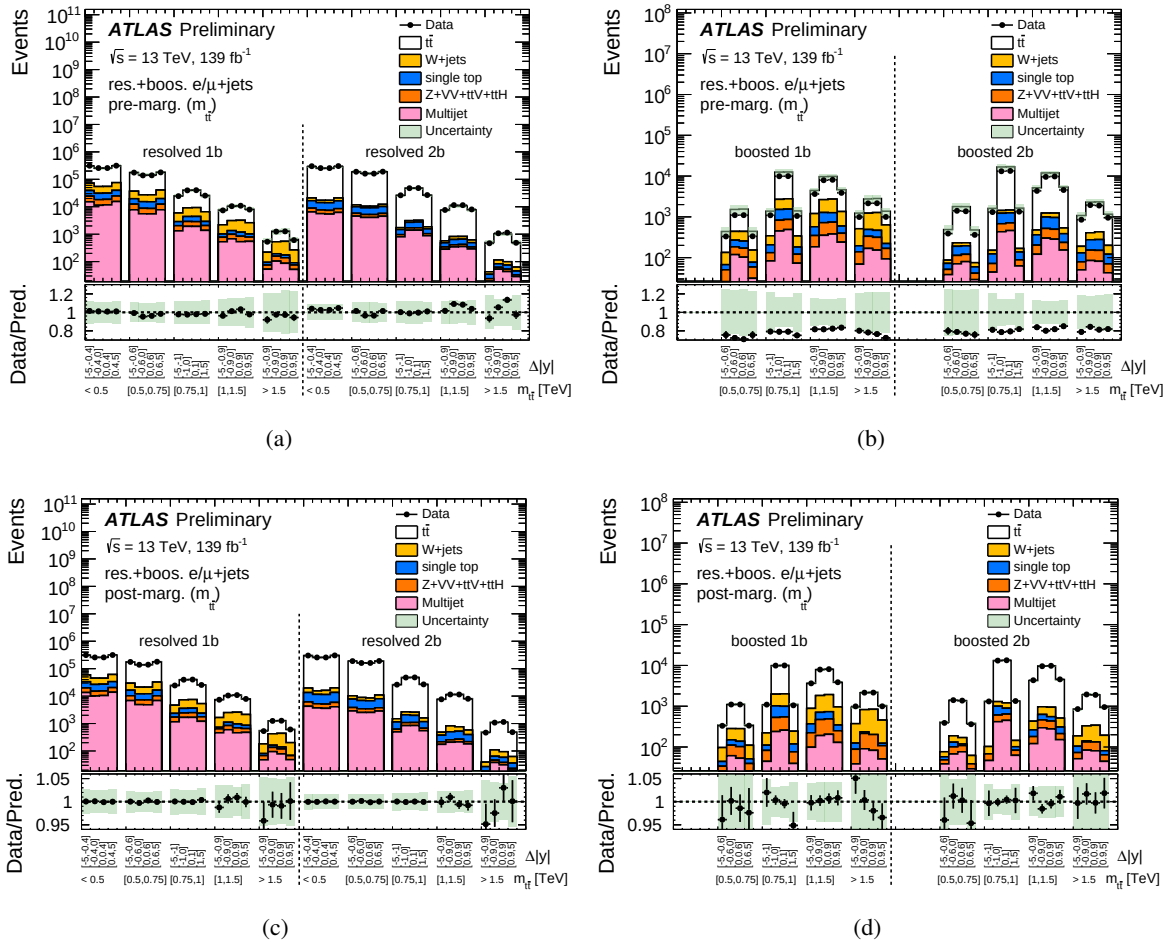

Figure 3: Comparison between the data and the prediction for bins used in the $m_{t\bar{t}}$ differential A_C measurements in the lepton+jets channel. This comparison is shown before (upper) and after (lower) marginalisation within FBU for resolved (left) and boosted (right) topology. The bottom panels show the ratio of data to the predictions. The light green bands correspond to the total uncertainty of the prediction.

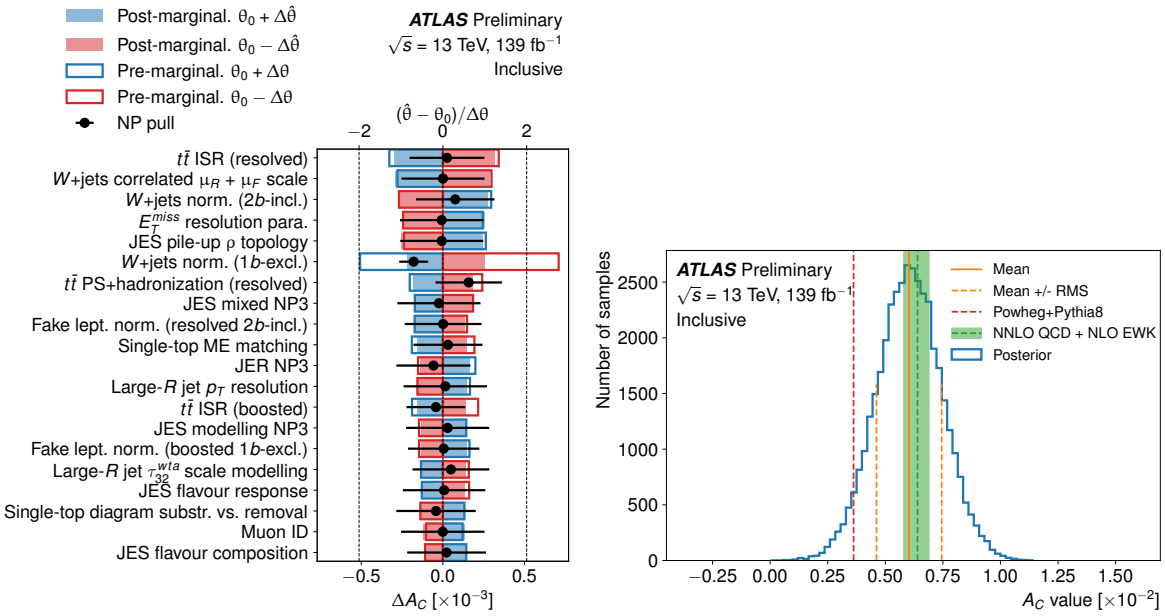

(a) (b)

Figure 4: (a) Ranking of the systematic uncertainties with marginalisation for the inclusive A_C measurement. Only the 20 highest ranking uncertainties are shown, ordered based on the post-marginalisation ranking, which considers the constraining power of the marginalisation for the Asimov dataset. The red and blue bars show the effect on unfolded A_C for down and up variation of the systematic uncertainty, respectively. The impact of each nuisance parameter, ΔA_C, is computed by comparing the nominal best-fit value, with the result of the fit when fixing the considered nuisance parameter to its best-fit value, $\hat{\theta}$, shifted by its pre-fit (post-fit) uncertainties $\pm\Delta\theta(\pm\Delta\hat{\theta})$. The black points show the pulls and constraints of the ranked NPs obtained from data. (b) A_C posteriors in the inclusive measurement. The SM prediction from the nominal $t\bar{t}$ signal sample and posterior mean values are represented in red dashed and orange continue lines, respectively.

8.2 Comparison with the Standard Model prediction

The SM prediction has been obtained by performing fixed-order calculations at NNLO in the perturbative expansion in the strong coupling constant of QCD, with NLO electro-weak corrections [129]. Fully differential results are available, including a detailed analysis of the charge asymmetry at the LHC [130, 131]. The same calculation is compared to Tevatron results for the forward-backward asymmetry [9, 132].

The predictions presented in the results are calculated using $m_{\text{top}} = 172.5$ GeV [133]. The PDF of the proton is taken from LUXqed17_plus_PDF4LHC15_nnlo_100. A dynamical renormalisation and factorisation scale [134] is used, with the nominal value μ_0 chosen as $H_T/4$, where $H_{\text{T}} = \sqrt{m_t^2 + p_{\text{T},t}^2} + \sqrt{m_{\bar{t}}^2 + p_{\text{T},\bar{t}}^2}$. The scale uncertainty band indicates the maximum and the minimum value of the asymmetry obtained under an independent variation of the scale by a factor of 2.0 around μ_0. The variations, in which one scale is reduced by a factor of 2.0 while the other scale is increased by a factor of 2.0, are excluded. The MC integration uncertainty is typically smaller than the scale uncertainty. Finally, the scale and MC integration uncertainties are added in quadrature.

Table 2 and figure 5 show a comparison of the measured asymmetry with the SM prediction and the nominal $t\bar{t}$ signal sample. The measured asymmetry is consistent with NNLO calculations [133].

		Data 139 fb^{-1}						SM prediction
		A_{C}	Stat.	Syst.	MC stat.	Bias	Total unc.	
Inclusive		0.0060	0.0011	0.0009	0.0005	0.0001	0.0015	$0.0064^{+0.0005}_{-0.0006}$
$m_{t\bar{t}}$	< 500 GeV	0.0045	0.0028	0.0034	0.0013	0.0001	0.0045	$0.0055^{+0.0007}_{-0.0005}$
	500-750 GeV	0.0051	0.0020	0.0021	0.0009	<0.0001	0.0031	$0.0072^{+0.0006}_{-0.0006}$
	750-1000 GeV	0.0100	0.0049	0.0046	0.0021	0.0001	0.0070	$0.0079^{+0.0003}_{-0.0005}$
	1000-1500 GeV	0.0169	0.0072	0.0027	0.0029	0.0004	0.0083	$0.0096^{+0.0009}_{-0.0009}$
	> 1500 GeV	0.0121	0.0277	0.0150	0.0092	0.0005	0.0329	$0.0094^{+0.0015}_{-0.0011}$
$\beta_{z,t\bar{t}}$	0-0.3	0.0007	0.0040	0.0032	0.0020	0.0001	0.0055	$0.0011^{+0.0004}_{-0.0004}$
	0.3-0.6	0.0085	0.0031	0.0025	0.0013	0.0003	0.0042	$0.0023^{+0.0006}_{-0.0004}$
	0.6-0.8	0.0014	0.0029	0.0033	0.0015	0.0004	0.0047	$0.0042^{+0.0003}_{-0.0003}$
	0.8-1.0	0.0100	0.0026	0.0042	0.0013	0.0007	0.0051	$0.0146^{+0.0012}_{-0.0014}$

Table 2: Results with statistical and systematic uncertainties, including the uncertainty due to limited number of MC events (MC stat. column), uncertainty due to the unfolding bias and the total uncertainty, for the inclusive and differential A_{C} measurements. The total uncertainty is the sum-in-quadrature of the aforementioned uncertainties. The SM predictions are calculated at NNLO in QCD and NLO in electroweak theory [133].

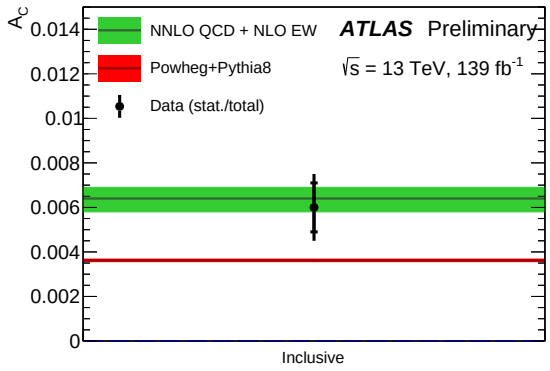

(a)

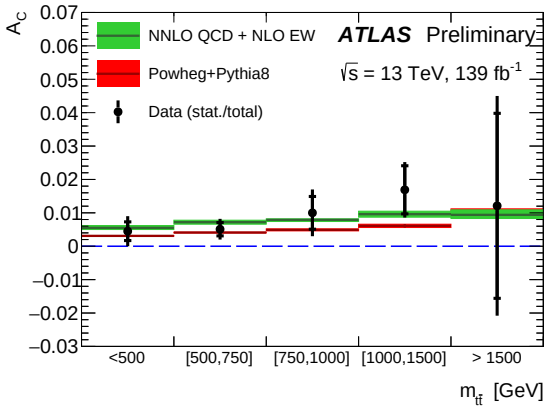

(b)

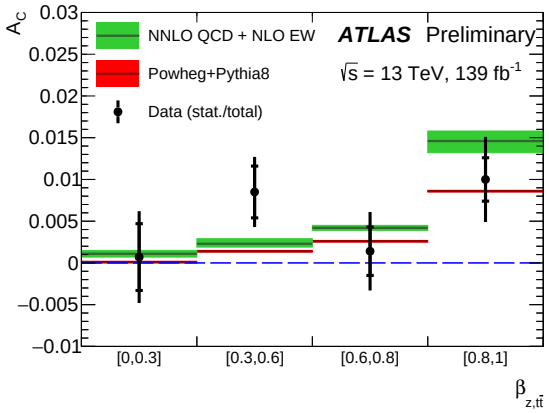

(c)

Figure 5: The unfolded inclusive (a) and differential charge asymmetries as a function of the invariant mass (b) and the longitudinal boost (c) of the top pair system in data (resolved and boosted topologies are combined). Green hatched regions show SM theory predictions calculated at NNLO in QCD and NLO in electroweak theory [133]. Red hatched regions show parton-level truth asymmetry with its uncertainty extracted from the full phase space using nominal $t\bar{t}$ signal sample. Vertical bars correspond to the total uncertainties.

8.3 EFT interpretation of the result

In this Section the charge asymmetry measurements are interpreted in the framework of an effective field theory (EFT). In EFT formalism the Standard Model Lagrangian is extended with dimension-six operators that encode the effect of new physics phenomena at a scale beyond the direct reach of the experiment. A general effective Lagrangian $\mathcal{L}_{eff}$ expands around the Standard Model in terms of a new physics scale Λ^{-2}:

$$\mathcal{L}_{eff} = \mathcal{L}_{SM} + \frac{1}{\Lambda^2}\sum_i C_i O_i + O\left(\Lambda^{-4}\right), \tag{7}$$

where $\mathcal{L}_{SM}$ is the usual "renormalizable" part of the SM Lagrangian, where O_i denote local $SU(3)_c \times SU(2)_L \times U(1)_Y$-invariant operators of mass dimension-six built from fields of the SM particle spectrum only, and C_i stand for the corresponding dimensionless coupling constants (Wilson coefficients) that encode

the virtual effects of BSM physics in low-energy observables.[5] For the expansion to hold the process characteristic transferred momentum should be small if compared with Λ: $|q^2| << \Lambda^2$.

The Warsaw basis comprises a complete set of dimension-six operators [135]. Charge asymmetry at hadron colliders is sensitive to seven four-fermion operators in the Warsaw basis, which is reduced to four by using a flavour-specific linear combination [136]:

$$\begin{aligned} C_u^1 &= C_{qq}^{(8,1)} + C_{qq}^{(8,3)} + C_{ut}^{(8)} \\ C_u^2 &= C_{qu}^{(1)} + C_{qt}^{(1)} \\ C_d^1 &= C_{qq}^{(8,1)} - C_{qq}^{(8,3)} + C_{dt}^{(8)} \\ C_d^2 &= C_{qd}^{(1)} + C_{qt}^{(1)} \end{aligned} \tag{8}$$

The operators are implemented in a UFO model [137] in the MadGraph_aMC@NLO package [95]. This interpretation is compatible with the standard basis [138], proposed by the LHC top physics working group.

The number of independent Wilson coefficients is reduced further by taking $C_u^1 = C_d^1 = C^1$ and $C_u^2 = C_d^2 = C^2$ [139]. This assumption of equal couplings to up- and down-type quarks is valid in models where the couplings are flavour-universal. It is also valid in many models that are not strictly flavour-universal, such as for an axigluon model with an opposite-sign coupling to light quarks and the top quark [2] or for Kaluza-Klein of Randall-Sundrum models with warped extra-dimensions [140, 141].

The $t\bar{t}$ production cross section at hadron colliders is sensitive to the linear combination $C^+ = C^1 + C^2$, while the charge asymmetry is affected by the difference $C^- = C^1 - C^2$. The limit on C^- can be recast as a bound on the coupling and mass of massive new states in a variety of models. The parameters of the axigluon, for instance, are related to C^- through the following simple relation [137]:

$$C^-/\Lambda^2 = -4g_s^2/m_A^2. \tag{9}$$

Bounds on C^-/Λ^2 are derived from the inclusive charge asymmetry measurement, and from each of the measurements in differential $m_{t\bar{t}}$ bins. First, a possible BSM contribution to the asymmetry is isolated by subtracting the value predicted by the Standard Model from the measurement.

The bounds extracted from several charge asymmetry measurements are compared in Fig. 6. Several measurements provide powerful constraints on C^-/Λ^2, with 68% C.L. bounds from individual measurements reaching well below 1 TeV^{-2}. Thanks to the total uncertainty of 0.15%, the inclusive measurement yields a very tight bound despite the strong dilution of the asymmetry due to symmetric gluon-gluon collisions. The sensitivity to the dimension-six operator increases strongly with increasing invariant mass of the $t\bar{t}$ system. Therefore, the measurement of the asymmetry in the mass range of 1000-1500 GeV, with a precision of 0.83%, yields an equally tight bound. Fig. 6 also displays the bounds, obtained with the same procedure, from the combined measurements of the CDF and D0 experiments [142] at the Tevatron, in $p\bar{p}$ collisions at 1.96 TeV, as well as the combination of ATLAS and CMS measurements [38] on $\sqrt{s} = 8$ TeV data. The 13 TeV data provide a considerably tighter bound than the combination of previous measurements.

[5] The lepton and baryon numbers are assumed to be conserved independently, then all relevant operators are of even dimension.

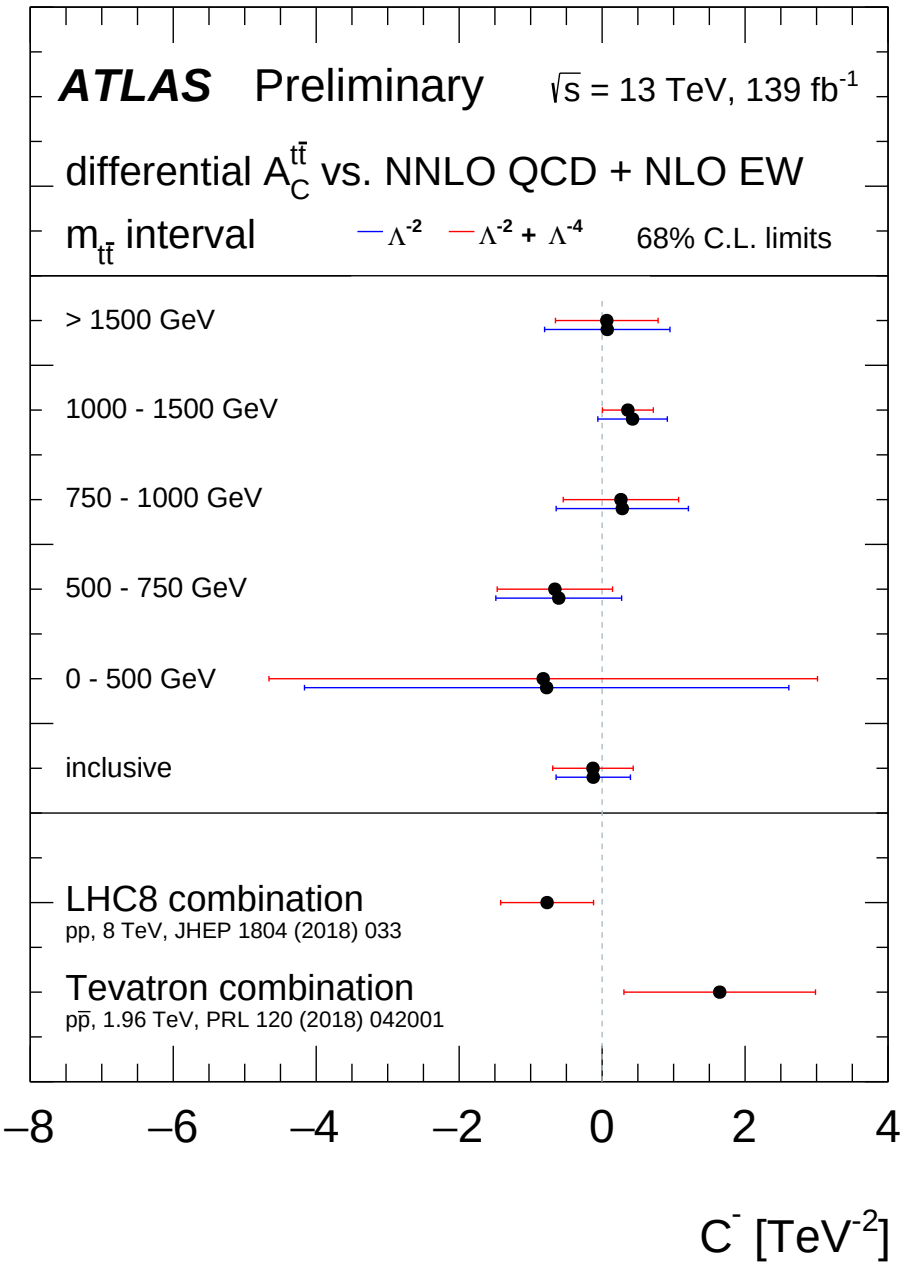

Figure 6: The 68% C.L. limits on the linear combination C^{-}/Λ^2 of Wilson coefficients of dimension-six operators. The bounds are derived from a comparison of the charge asymmetry measurements presented in this paper with the Standard Model predictions of the NNLO QCD + NLO EW calculation [129]. The impact of dimension-six operators is parameterised [139]. Bounds are also shown from the forward-backward asymmetry measurements in $p\bar{p}$ collisions at $\sqrt{s}$ = 1.96 TeV at the Tevatron and the charge asymmetry measurements in pp collisions at a center-of-mass energy of 8 TeV in LHC run 1.

9 Conclusion

The charge asymmetry in top quark pair production is measured in the lepton+jets decay channel using 139 fb^{-1}of data collected by the ATLAS experiment at $\sqrt{s}$ = 13 TeV. A fully Bayesian unfolding method is used to correct for detector resolution and acceptance effects. The resolved and boosted topologies are unfolded simultaneously. Differential measurements are performed as a function of the invariant mass and of the longitudinal boost of the $t\bar{t}$ system. In comparison with previous results obtained at 8 TeV, the differential variables benefit from a finer binning at larger values which are sensitive to possible enhancements of the charge asymmetry due to new physics beyond the Standard model. The asymmetry obtained in the inclusive measurement is found to differ from zero by four standard deviations and is measured as $A_C = 0.0060 \pm 0.0015$(stat+syst.). The inclusive and differential measurements are consistent with the Standard Model predictions calculated at next-to-next-to-leading-order in quantum chromodynamics and next-to-leading order in electroweak theory.

The results are interpreted in the framework of an effective field theory. 68% C.L. limits on the linear combination of Wilson coefficients for dimension-six operators, C^-/Λ^2, are derived from the inclusive charge asymmetry measurement, and from each of the measurements in $m_{t\bar{t}}$ bins. The measured data provide considerably tighter bounds than the combination of previous measurements.

References

[1] ATLAS Collaboration, *Measurement of the $t\bar{t}$ production cross-section using $e\mu$ events with b-tagged jets in pp collisions at $\sqrt{s}$ = 13 TeV with the ATLAS detector*, Phys. Lett. B **761** (2016) 136, arXiv: 1606.02699 [hep-ex] (cit. on p. 2).

[2] O. Antunano, J. H. Kuhn and G. Rodrigo, *Top quarks, axigluons and charge asymmetries at hadron colliders*, Phys. Rev. D **77** (2008) 014003, arXiv: 0709.1652 [hep-ph] (cit. on pp. 2, 22).

[3] J. L. Rosner, *Prominent decay modes of a leptophobic Z'*, Phys. Lett. B **387** (1996) 113, arXiv: hep-ph/9607207 [hep-ph] (cit. on p. 2).

[4] P. Ferrario and G. Rodrigo, *Massive color-octet bosons and the charge asymmetries of top quarks at hadron colliders*, Phys. Rev. D **78** (2008) 094018, arXiv: 0809.3354 [hep-ph] (cit. on p. 2).

[5] J. H. Kuhn and G. Rodrigo, *Charge asymmetry of heavy quarks at hadron colliders*, Phys. Rev. D **59** (1999) 054017, arXiv: hep-ph/9807420 [hep-ph] (cit. on p. 2).

[6] J. H. Kuhn and G. Rodrigo, *Charge asymmetries of top quarks at hadron colliders revisited*, JHEP **01** (2012) 063, arXiv: 1109.6830 [hep-ph] (cit. on p. 2).

[7] W. Bernreuther and Z.-G. Si, *Top quark and leptonic charge asymmetries for the Tevatron and LHC*, Phys. Rev. D **86** (2012) 034026, arXiv: 1205.6580 [hep-ph] (cit. on p. 2).

[8] J. A. Aguilar-Saavedra, D. Amidei, A. Juste and M. Perez-Victoria, *Asymmetries in top quark pair production at hadron colliders*, Rev. Mod. Phys. **87** (2015) 421, arXiv: 1406.1798 [hep-ph] (cit. on p. 2).

[9] M. Czakon, P. Fiedler and A. Mitov, *Resolving the Tevatron Top Quark Forward-Backward Asymmetry Puzzle: Fully Differential Next-to-Next-to-Leading-Order Calculation*, Phys. Rev. Lett. **115** (2015) 052001, arXiv: 1411.3007 [hep-ph] (cit. on pp. 2, 20).

[10] T. Aaltonen et al., *Forward-Backward Asymmetry in Top Quark Production in $p\bar{p}$ Collisions at $\sqrt{s} = 1.96$ TeV*, Phys. Rev. Lett. **101** (2008) 202001, arXiv: 0806.2472 [hep-ex] (cit. on p. 2).

[11] V. M. Abazov et al., *First measurement of the forward-backward charge asymmetry in top quark pair production*, Phys. Rev. Lett. **100** (2008) 142002, arXiv: 0712.0851 [hep-ex] (cit. on p. 2).

[12] S. Jung, A. Pierce and J. D. Wells, *Top quark asymmetry from a non-Abelian horizontal symmetry*, Phys. Rev. D **83** (2011) 114039, arXiv: 1103.4835 [hep-ph] (cit. on p. 2).

[13] R. Diener, S. Godfrey and T. A. W. Martin, *Using Final State Pseudorapidities to Improve s-channel Resonance Observables at the LHC*, Phys. Rev. D **80** (2009) 075014, arXiv: 0909.2022 [hep-ph] (cit. on p. 2).

[14] A. Djouadi, G. Moreau, F. Richard and R. K. Singh, *The Forward-backward asymmetry of top quark production at the Tevatron in warped extra dimensional models*, Phys. Rev. D **82** (2010) 071702, arXiv: 0906.0604 [hep-ph] (cit. on p. 2).

[15] S. Jung, H. Murayama, A. Pierce and J. D. Wells, *Top quark forward-backward asymmetry from new t-channel physics*, Phys. Rev. D **81** (2010) 015004, arXiv: 0907.4112 [hep-ph] (cit. on p. 2).

[16] P. H. Frampton, J. Shu and K. Wang, *Axigluon as Possible Explanation for $p\bar{p} \to t\bar{t}$ Forward-Backward Asymmetry*, Phys. Lett. B **683** (2010) 294, arXiv: 0911.2955 [hep-ph] (cit. on p. 2).

[17] P. Ferrario and G. Rodrigo, *Constraining heavy colored resonances from top-antitop quark events*, Phys. Rev. D **80** (2009) 051701, arXiv: 0906.5541 [hep-ph] (cit. on p. 2).

[18] B. Grinstein, A. L. Kagan, M. Trott and J. Zupan, *Forward-backward asymmetry in $t\bar{t}$ production from flavour symmetries*, Phys. Rev. Lett. **107** (2011) 012002, arXiv: 1102.3374 [hep-ph] (cit. on p. 2).

[19] J. A. Aguilar-Saavedra and M. Perez-Victoria, *Asymmetries in $t\,\bar{t}$ production: LHC versus Tevatron*, Phys. Rev. D **84** (2011) 115013, arXiv: 1105.4606 [hep-ph] (cit. on p. 2).

[20] Z. Ligeti, G. Marques Tavares and M. Schmaltz, *Explaining the $t\bar{t}$ forward-backward asymmetry without dijet or flavor anomalies*, JHEP **06** (2011) 109, arXiv: 1103.2757 [hep-ph] (cit. on p. 2).

[21] J. A. Aguilar-Saavedra and M. Perez-Victoria, *Probing the Tevatron $t\bar{t}$ asymmetry at LHC*, JHEP **05** (2011) 034, arXiv: 1103.2765 [hep-ph] (cit. on p. 2).

[22] J. A. Aguilar-Saavedra, A. Juste and F. Rubbo, *Boosting the $t\bar{t}$ charge asymmetry*, Phys. Lett. B **707** (2012) 92, arXiv: 1109.3710 [hep-ph] (cit. on p. 2).

[23] T. Aaltonen et al., *Evidence for a Mass Dependent Forward-Backward Asymmetry in Top Quark Pair Production*, Phys. Rev. D **83** (2011) 112003, arXiv: 1101.0034 [hep-ex] (cit. on p. 2).

[24] V. M. Abazov et al., *Simultaneous measurement of forward-backward asymmetry and top polarization in dilepton final states from $t\bar{t}$ production at the Tevatron*, Phys. Rev. D **92** (2015) 052007, arXiv: 1507.05666 [hep-ex] (cit. on p. 2).

[25] T. Aaltonen et al., *Measurement of the top quark forward-backward production asymmetry and its dependence on event kinematic properties*, Phys. Rev. D **87** (2013) 092002, arXiv: 1211.1003 [hep-ex] (cit. on p. 2).

[26] V. M. Abazov et al., *Measurement of the Forward-Backward Asymmetry in Top Quark-Antiquark Production in $p\bar{p}$ Collisions using the Lepton+Jets Channel*, Phys. Rev. D **90** (2014) 072011, arXiv: 1405.0421 [hep-ex] (cit. on p. 2).

[27] ATLAS Collaboration, *Measurement of the top quark pair production charge asymmetry in proton–proton collisions at $\sqrt{s}$ = 7 TeV using the ATLAS detector*, JHEP **02** (2014) 107, arXiv: 1311.6724 [hep-ex] (cit. on p. 3).

[28] ATLAS Collaboration, *Measurement of the charge asymmetry in top-quark pair production in the lepton-plus-jets final state in pp collision data at $\sqrt{s}$ = 8 TeV with the ATLAS detector*, Eur. Phys. J. C **76** (2016) 87, arXiv: 1509.02358 [hep-ex] (cit. on p. 3).

[29] CMS Collaboration, *Inclusive and differential measurements of the $t\bar{t}$ charge asymmetry in proton–proton collisions at $\sqrt{s}$ = 7 TeV*, Phys. Lett. B **717** (2012) 129, arXiv: 1207.0065 [hep-ex] (cit. on p. 3).

[30] CMS Collaboration, *Inclusive and differential measurements of the $t\bar{t}$ charge asymmetry in pp collisions at $\sqrt{s}$ = 8 TeV*, Phys. Lett. B **757** (2016) 154, arXiv: 1507.03119 [hep-ex] (cit. on p. 3).

[31] ATLAS Collaboration, *Measurement of the charge asymmetry in dileptonic decays of top quark pairs in pp collisions at $\sqrt{s}$ = 7 TeV using the ATLAS detector*, JHEP **05** (2015) 061, arXiv: 1501.07383 [hep-ex] (cit. on p. 3).

[32] ATLAS Collaboration, *Measurements of the charge asymmetry in top-quark pair production in the dilepton final state at $\sqrt{s}$ = 8 TeV with the ATLAS detector*, Phys. Rev. D **94** (2016) 032006, arXiv: 1604.05538 [hep-ex] (cit. on p. 3).

[33] CMS Collaboration, *Measurements of the $t\bar{t}$ charge asymmetry using the dilepton decay channel in pp collisions at $\sqrt{s}$ = 7 TeV*, JHEP **04** (2014) 191, arXiv: 1402.3803 [hep-ex] (cit. on p. 3).

[34] CMS Collaboration, *Measurements of $t\bar{t}$ charge asymmetry using dilepton final states in pp collisions at $\sqrt{s}$ = 8 TeV*, Phys. Lett. B **760** (2016) 365, arXiv: 1603.06221 [hep-ex] (cit. on p. 3).

[35] ATLAS Collaboration, *Measurement of the charge asymmetry in highly boosted top-quark pair production in $\sqrt{s}$ = 8 TeV pp collision data collected by the ATLAS experiment*, Phys. Lett. B **756** (2016) 52, arXiv: 1512.06092 [hep-ex] (cit. on p. 3).

[36] CMS Collaboration, *Measurement of the charge asymmetry in top quark pair production in pp collisions at $\sqrt{s}$ = 8 TeV using a template method*, Phys. Rev. D **93** (2016) 034014, arXiv: 1508.03862 [hep-ex] (cit. on p. 3).

[37] CMS Collaboration, *Measurements of $t\bar{t}$ differential cross sections in proton–proton collisions at $\sqrt{s}$ = 13 TeV using events containing two leptons*, JHEP **02** (2019) 149, arXiv: 1811.06625 [hep-ex] (cit. on p. 3).

[38] ATLAS and CMS Collaborations, *Combination of inclusive and differential $t\bar{t}$ charge asymmetry measurements using ATLAS and CMS data at $\sqrt{s}$ = 7 TeV and 8 TeV*, JHEP **04** (2018) 033, arXiv: 1709.05327 [hep-ex] (cit. on pp. 3, 22).

[39] G.Choudalakis, *Fully Bayesian Unfolding*, (2012), arXiv: 1201.4612 [hep-ex] (cit. on pp. 3, 11).

[40] ATLAS Collaboration, *The ATLAS Experiment at the CERN Large Hadron Collider*, JINST **3** (2008) S08003 (cit. on p. 3).

[41] ATLAS Collaboration, *ATLAS Insertable B-Layer Technical Design Report*, ATLAS-TDR-19, 2010, URL: https://cds.cern.ch/record/1291633 (cit. on p. 3), Addendum: ATLAS-TDR-19-ADD-1, 2012, URL: https://cds.cern.ch/record/1451888.

[42] B. Abbott et al., *Production and integration of the ATLAS Insertable B-Layer*, JINST **13** (2018) T05008, arXiv: 1803.00844 [physics.ins-det] (cit. on p. 3).

[43] ATLAS Collaboration, *Performance of the ATLAS trigger system in 2015*, Eur. Phys. J. C **77** (2017) 317, arXiv: 1611.09661 [hep-ex] (cit. on p. 4).

[44] ATLAS Collaboration, *Vertex Reconstruction Performance of the ATLAS Detector at* $\sqrt{s}$ = 13 *TeV*, ATL-PHYS-PUB-2015-026, 2015, URL: https://cds.cern.ch/record/2037717 (cit. on p. 4).

[45] ATLAS Collaboration, *Electron reconstruction and identification in the ATLAS experiment using the 2015 and 2016 LHC proton-proton collision data at* $\sqrt{s}$ = *13 TeV*, Submitted to: Eur. Phys. J. (2019), arXiv: 1902.04655 [physics.ins-det] (cit. on pp. 4, 12).

[46] ATLAS Collaboration, *Muon reconstruction performance of the ATLAS detector in proton–proton collision data at* $\sqrt{s}$ =*13 TeV*, Eur. Phys. J. C **76** (2016) 292, arXiv: 1603.05598 [hep-ex] (cit. on p. 4).

[47] M. Cacciari, G. P. Salam and G. Soyez, *The Anti-k(t) jet clustering algorithm*, JHEP **04** (2008) 063, arXiv: 0802.1189 [hep-ph] (cit. on pp. 4, 5).

[48] W. Lampl et al., *Calorimeter Clustering Algorithms: Description and Performance*, tech. rep. ATL-LARG-PUB-2008-002. ATL-COM-LARG-2008-003, CERN, 2008, URL: https://cds.cern.ch/record/1099735 (cit. on p. 4).

[49] M. Cacciari, G. P. Salam and G. Soyez, *The catchment area of jets*, JHEP **04** (2008) 005, arXiv: 0802.1188 [hep-ph] (cit. on p. 4).

[50] ATLAS Collaboration, *Jet energy scale measurements and their systematic uncertainties in proton–proton collisions at* $\sqrt{s}$ = 13 *TeV with the ATLAS detector*, Phys. Rev. D **96** (2017) 072002, arXiv: 1703.09665 [hep-ex] (cit. on pp. 4, 5, 12).

[51] ATLAS Collaboration, *Performance of pile-up mitigation techniques for jets in pp collisions at* $\sqrt{s}$ = 8 *TeV using the ATLAS detector*, Eur. Phys. J. C **76** (2016) 581, arXiv: 1510.03823 [hep-ex] (cit. on p. 4).

[52] ATLAS Collaboration, *Optimisation and performance studies of the ATLAS b-tagging algorithms for the 2017-18 LHC run*, ATL-PHYS-PUB-2017-013, 2017, URL: https://cds.cern.ch/record/2273281 (cit. on p. 4).

[53] ATLAS Collaboration, *Measurements of b-jet tagging efficiency with the ATLAS detector using* $t\bar{t}$ *events at* $\sqrt{s}$ = 13 *TeV*, JHEP **08** (2018) 089, arXiv: 1805.01845 [hep-ex] (cit. on pp. 4, 5, 12).

[54] ATLAS Collaboration, *Measurement of b-tagging efficiency of c-jets in* $t\bar{t}$ *events using a likelihood approach with the ATLAS detector*, ATLAS-CONF-2018-001, 2018, URL: https://cds.cern.ch/record/2306649 (cit. on pp. 5, 12).

[55] ATLAS Collaboration, *Topological cell clustering in the ATLAS calorimeters and its performance in LHC Run 1*, Eur. Phys. J. C **77** (2017) 490, arXiv: 1603.02934 [hep-ex] (cit. on p. 5).

[56] ATLAS Collaboration, *Jet energy measurement and its systematic uncertainty in proton–proton collisions at* $\sqrt{s}$ = 7 *TeV with the ATLAS detector*, Eur. Phys. J. C **75** (2015) 17, arXiv: 1406.0076 [hep-ex] (cit. on p. 5).

[57] D. Krohn, J. Thaler and L.-T. Wang, *Jet Trimming*, JHEP **02** (2010) 084, arXiv: 0912.1342 [hep-ph] (cit. on p. 5).

[58] S. D. Ellis and D. E. Soper, *Successive combination jet algorithm for hadron collisions*, Phys. Rev. D **48** (1993) 3160, arXiv: hep-ph/9305266 [hep-ph] (cit. on p. 5).

[59] ATLAS Collaboration, *Identification of boosted, hadronically decaying W bosons and comparisons with ATLAS data taken at* $\sqrt{s} = 8$ *TeV*, Eur. Phys. J. C **76** (2016) 154, arXiv: 1510.05821 [hep-ex] (cit. on pp. 5, 12).

[60] J. Thaler and K. Van Tilburg, *Identifying Boosted Objects with N-subjettiness*, JHEP **03** (2011) 015, arXiv: 1011.2268 [hep-ph] (cit. on pp. 5, 7).

[61] ATLAS collaboration, *Performance of missing transverse momentum reconstruction with the ATLAS detector using proton-proton collisions at* $\sqrt{s} = 13$ *TeV*, Eur. Phys. J. C **78** (2018) 903, arXiv: 1802.08168 [hep-ex] (cit. on pp. 5, 13).

[62] A. Hoecker et al., *TMVA: Toolkit for Multivariate Data Analysis*, PoS **ACAT** (2007) 040, arXiv: physics/0703039 (cit. on p. 6).

[63] J. Erdmann et al., *A likelihood-based reconstruction algorithm for top-quark pairs and the KLFitter framework*, Nucl. Instrum. Meth. A **748** (2014) 18, arXiv: 1312.5595 [hep-ex] (cit. on p. 6).

[64] ATLAS Collaboration, *Performance of Top Quark and W Boson Tagging in Run 2 with ATLAS*, ATLAS-CONF-2017-064, 2017, URL: https://cds.cern.ch/record/2281054 (cit. on p. 7).

[65] D. J. Lange, *The EvtGen particle decay simulation package*, Nucl. Instrum. Meth. A **462** (2001) 152 (cit. on p. 7).

[66] E. Bothmann et al., *Event Generation with Sherpa 2.2*, (2019), arXiv: 1905.09127 [hep-ph] (cit. on pp. 7, 9, 10).

[67] S. Agostinelli et al., *Geant4a simulation toolkit*, Nuclear Instruments and Methods in Physics Research Section A: Accelerators, Spectrometers, Detectors and Associated Equipment **506** (2003) 250, ISSN: 0168-9002, URL: http://www.sciencedirect.com/science/article/pii/S0168900203013688 (cit. on p. 7).

[68] E. Richter-Was, D. Froidevaux and L. Poggioli, *ATLFAST 2.0 a fast simulation package for ATLAS*, tech. rep. ATL-PHYS-98-131, CERN, 1998, URL: https://cds.cern.ch/record/683751 (cit. on p. 8).

[69] T. Sjöstrand et al., *An Introduction to PYTHIA 8.2*, Comput. Phys. Commun. **191** (2015) 159, arXiv: 1410.3012 [hep-ph] (cit. on pp. 8–10).

[70] A. D. Martin, W. J. Stirling, R. S. Thorne and G. Watt, *Parton distributions for the LHC*, Eur. Phys. J. C **63** (2009) 189, arXiv: 0901.0002 [hep-ph] (cit. on p. 8).

[71] ATLAS Collaboration, *The Pythia 8 A3 tune description of ATLAS minimum bias and inelastic measurements incorporating the Donnachie–Landshoff diffractive model*, ATL-PHYS-PUB-2016-017, 2016, URL: https://cds.cern.ch/record/2206965 (cit. on p. 8).

[72] M. Beneke, P. Falgari, S. Klein and C. Schwinn, *Hadronic top-quark pair production with NNLL threshold resummation*, Nucl. Phys. B **855** (2012) 695, arXiv: 1109.1536 [hep-ph] (cit. on p. 8).

[73] M. Cacciari, M. Czakon, M. Mangano, A. Mitov and P. Nason, *Top-pair production at hadron colliders with next-to-next-to-leading logarithmic soft-gluon resummation*, Phys. Lett. B **710** (2012) 612, arXiv: 1111.5869 [hep-ph] (cit. on p. 8).

[74] P. Bärnreuther, M. Czakon and A. Mitov, *Percent Level Precision Physics at the Tevatron: First Genuine NNLO QCD Corrections to* $q\bar{q} \to t\bar{t} + X$, Phys. Rev. Lett. **109** (2012) 132001, arXiv: 1204.5201 [hep-ph] (cit. on p. 8).

[75] M. Czakon and A. Mitov, *NNLO corrections to top-pair production at hadron colliders: the all-fermionic scattering channels*, JHEP **12** (2012) 054, arXiv: 1207.0236 [hep-ph] (cit. on p. 8).

[76] M. Czakon and A. Mitov, *NNLO corrections to top pair production at hadron colliders: the quark-gluon reaction*, JHEP **01** (2013) 080, arXiv: 1210.6832 [hep-ph] (cit. on p. 8).

[77] M. Czakon, P. Fiedler and A. Mitov, *The total top quark pair production cross-section at hadron colliders through $O(\alpha_S^4)$*, Phys. Rev. Lett. **110** (2013) 252004, arXiv: 1303.6254 [hep-ph] (cit. on p. 8).

[78] M. Czakon and A. Mitov, *Top++: A Program for the Calculation of the Top-Pair Cross-Section at Hadron Colliders*, Comput. Phys. Commun. **185** (2014) 2930, arXiv: 1112.5675 [hep-ph] (cit. on p. 8).

[79] M. Botje et al., *The PDF4LHC Working Group Interim Recommendations*, (2011), arXiv: 1101.0538 [hep-ph] (cit. on p. 8).

[80] A. D. Martin, W. Stirling, R. Thorne and G. Watt, *Uncertainties on α_S in global PDF analyses and implications for predicted hadronic cross sections*, Eur. Phys. J. C **64** (2009) 653, arXiv: 0905.3531 [hep-ph] (cit. on p. 8).

[81] H.-L. Lai et al., *New parton distributions for collider physics*, Phys. Rev. D **82** (2010) 074024, arXiv: 1007.2241 [hep-ph] (cit. on p. 8).

[82] J. Gao, M. Guzzi, J. Huston, H.-L. Lai, Z. Li et al., *The CT10 NNLO Global Analysis of QCD*, Phys. Rev. D **89** (2014) 033009, arXiv: 1302.6246 [hep-ph] (cit. on p. 8).

[83] R. D. Ball, V. Bertone, S. Carrazza, C. S. Deans, L. Del Debbio et al., *Parton distributions with LHC data*, Nucl. Phys. B **867** (2013) 244, arXiv: 1207.1303 [hep-ph] (cit. on p. 8).

[84] S. Frixione, P. Nason and G. Ridolfi, *A Positive-weight next-to-leading-order Monte Carlo for heavy flavour hadroproduction*, JHEP **09** (2007) 126, arXiv: 0707.3088 [hep-ph] (cit. on pp. 8, 10).

[85] P. Nason, *A New method for combining NLO QCD with shower Monte Carlo algorithms*, JHEP **11** (2004) 040, arXiv: hep-ph/0409146 (cit. on pp. 8–10).

[86] S. Frixione, P. Nason and C. Oleari, *Matching NLO QCD computations with Parton Shower simulations: the POWHEG method*, JHEP **11** (2007) 070, arXiv: 0709.2092 [hep-ph] (cit. on pp. 8–10).

[87] S. Alioli, P. Nason, C. Oleari and E. Re, *A general framework for implementing NLO calculations in shower Monte Carlo programs: the POWHEG BOX*, JHEP **06** (2010) 043, arXiv: 1002.2581 [hep-ph] (cit. on pp. 8–10).

[88] R. D. Ball et al., *Parton distributions for the LHC Run II*, JHEP **04** (2015) 040, arXiv: 1410.8849 [hep-ph] (cit. on pp. 8–10).

[89] ATLAS Collaboration, *Studies on top-quark Monte Carlo modelling for Top2016*, ATL-PHYS-PUB-2016-020, 2016, URL: https://cds.cern.ch/record/2216168 (cit. on pp. 8, 9).

[90] ATLAS Collaboration, *ATLAS Pythia 8 tunes to 7 TeV data*, ATL-PHYS-PUB-2014-021, 2014, URL: https://cds.cern.ch/record/1966419 (cit. on pp. 8–10).

[91] ATLAS Collaboration, *Studies on top-quark Monte Carlo modelling with Sherpa and MG5_aMC@NLO*, ATL-PHYS-PUB-2017-007, 2017, URL: https://cds.cern.ch/record/2261938 (cit. on p. 8).

[92] M. Bahr et al., *Herwig++ Physics and Manual*, Eur. Phys. J. C **58** (2008) 639, arXiv: 0803.0883 [hep-ph] (cit. on pp. 8, 9).

[93] J. Bellm et al., *Herwig 7.0/Herwig++ 3.0 release note*, Eur. Phys. J. C **76** (2016) 196, arXiv: 1512.01178 [hep-ph] (cit. on pp. 8, 9).

[94] L. A. Harland-Lang, A. D. Martin, P. Motylinski and R. S. Thorne, *Parton distributions in the LHC era: MMHT 2014 PDFs*, Eur. Phys. J. C **75** (2015) 204, arXiv: 1412.3989 [hep-ph] (cit. on pp. 8, 9).

[95] J. Alwall et al., *The automated computation of tree-level and next-to-leading order differential cross sections, and their matching to parton shower simulations*, JHEP **07** (2014) 079, arXiv: 1405.0301 [hep-ph] (cit. on pp. 8, 22).

[96] J. A. Aguilar-Saavedra, *Single top quark production at LHC with anomalous Wtb couplings*, Nucl. Phys. B **804** (2008) 160, arXiv: 0803.3810 [hep-ph] (cit. on p. 9).

[97] E. Re, *Single-top Wt-channel production matched with parton showers using the POWHEG method*, Eur. Phys. J. C **71** (2011) 1547, arXiv: 1009.2450 [hep-ph] (cit. on pp. 9, 13, 14).

[98] S. Frixione, E. Laenen, P. Motylinski, B. R. Webber and C. D. White, *Single-top hadroproduction in association with a W boson*, JHEP **07** (2008) 029, arXiv: 0805.3067 [hep-ph] (cit. on p. 9).

[99] R. Frederix, E. Re and P. Torrielli, *Single-top t-channel hadroproduction in the four-flavour scheme with POWHEG and aMC@NLO*, JHEP **09** (2012) 130, arXiv: 1207.5391 [hep-ph] (cit. on p. 9).

[100] S. Alioli, P. Nason, C. Oleari and E. Re, *NLO single-top production matched with shower in POWHEG: s- and t-channel contributions*, JHEP **09** (2009) 111, [Erratum: JHEP 02 (2010) 011], arXiv: 0907.4076 [hep-ph] (cit. on p. 9).

[101] T. Gleisberg and S. Höche, *Comix, a new matrix element generator*, JHEP **12** (2008) 039, arXiv: 0808.3674 [hep-ph] (cit. on pp. 9, 10).

[102] F. Cascioli, P. Maierhofer and S. Pozzorini, *Scattering Amplitudes with Open Loops*, Phys. Rev. Lett. **108** (2012) 111601, arXiv: 1111.5206 [hep-ph] (cit. on pp. 9, 10).

[103] A. Denner, S. Dittmaier and L. Hofer, *Collier: a fortran-based Complex One-Loop LIbrary in Extended Regularizations*, Comput. Phys. Commun. **212** (2017) 220, arXiv: 1604.06792 [hep-ph] (cit. on pp. 9, 10).

[104] S. Schumann and F. Krauss, *A Parton shower algorithm based on Catani-Seymour dipole factorisation*, JHEP **03** (2008) 038, arXiv: 0709.1027 [hep-ph] (cit. on pp. 9, 10).

[105] J.-C. Winter, F. Krauss and G. Soff, *A Modified cluster hadronization model*, Eur. Phys. J. C **36** (2004) 381, arXiv: hep-ph/0311085 [hep-ph] (cit. on p. 10).

[106] C. Anastasiou, L. J. Dixon, K. Melnikov and F. Petriello, *High precision QCD at hadron colliders: Electroweak gauge boson rapidity distributions at NNLO*, Phys. Rev. D **69** (2004) 094008, arXiv: hep-ph/0312266 (cit. on p. 10).

[107] ATLAS Collaboration, *Estimation of non-prompt and fake lepton backgrounds in final states with top quarks produced in proton–proton collisions at $\sqrt{s}$ = 8 TeV with the ATLAS Detector*, ATLAS-CONF-2014-058, 2014, URL: https://cds.cern.ch/record/1951336 (cit. on p. 10).

[108] S. Hoeche, F. Krauss, M. Schonherr and F. Siegert, *A critical appraisal of NLO+PS matching methods*, JHEP **09** (2012) 049, arXiv: 1111.1220 [hep-ph] (cit. on p. 10).

[109] S. Catani, F. Krauss, R. Kuhn and B. R. Webber, *QCD matrix elements + parton showers*, JHEP **11** (2001) 063, arXiv: hep-ph/0109231 (cit. on pp. 10, 13).

[110] S. Höche, F. Krauss, S. Schumann and F. Siegert, *QCD matrix elements and truncated showers*, JHEP **05** (2009) 053, arXiv: 0903.1219 [hep-ph] (cit. on p. 10).

[111] S. Hoeche, F. Krauss, M. Schonherr and F. Siegert, *QCD matrix elements + parton showers: The NLO case*, JHEP **04** (2013) 027, arXiv: 1207.5030 [hep-ph] (cit. on p. 10).

[112] ATLAS Collaboration, *Luminosity Determination in pp Collisions at $\sqrt{s}$ = 13 TeV using the ATLAS Detector at the LHC*, ATLAS-CONF-2019-021, 2019, URL: https://cdsweb.cern.ch/record/2677054 (cit. on p. 12).

[113] G. Avoni et al., *The new LUCID-2 detector for luminosity measurement and monitoring in ATLAS*, JINST **13** (2018) P07017 (cit. on p. 12).

[114] ATLAS Collaboration, *Luminosity determination in pp collisions at $\sqrt{s}$ = 8 TeV using the ATLAS detector at the LHC*, Eur. Phys. J. C **76** (2016) 653, arXiv: 1608.03953 [hep-ex] (cit. on p. 12).

[115] ATLAS Collaboration, *Muon reconstruction performance of the ATLAS detector in proton–proton collision data at $\sqrt{s}$ = 13 TeV*, Eur. Phys. J. C **76** (2016) 292, arXiv: 1603.05598 [hep-ex] (cit. on p. 12).

[116] ATLAS Collaboration, *Electron and photon energy calibration with the ATLAS detector using LHC Run 1 data*, Eur. Phys. J. C **74** (2014) 3071, arXiv: 1407.5063 [hep-ex] (cit. on p. 12).

[117] ATLAS Collaboration, *Tagging and suppression of pileup jets with the ATLAS detector*, ATLAS-CONF-2014-018, 2014, URL: https://cds.cern.ch/record/1700870 (cit. on p. 12).

[118] ATLAS Collaboration, *Jet Calibration and Systematic Uncertainties for Jets Reconstructed in the ATLAS Detector at $\sqrt{s}$ = 13 TeV*, ATL-PHYS-PUB-2015-015, 2015, URL: https://cds.cern.ch/record/2037613 (cit. on p. 12).

[119] ATLAS Collaboration, *In-situ measurements of the ATLAS large-radius jet response in 13 TeV pp collisions*, ATLAS-CONF-2017-063, 2017, URL: https://cds.cern.ch/record/2275655 (cit. on p. 12).

[120] ATLAS Collaboration, *Calibration of light-flavour b-jet mistagging rates using ATLAS proton–proton collision data at $\sqrt{s}$ = 13 TeV*, ATLAS-CONF-2018-006, 2018, URL: https://cds.cern.ch/record/2314418 (cit. on p. 12).

[121] J. Rojo, *PDF4LHC recommendations for Run II*, PoS **DIS2016** (2016) 018, arXiv: 1606.08243 [hep-ph] (cit. on p. 13).

[122] ATLAS Collaboration, *ATLAS simulation of boson plus jets processes in Run 2*, ATL-PHYS-PUB-2017-006, 2017, URL: https://cds.cern.ch/record/2261937 (cit. on p. 13).

[123] F. Krauss, *Matrix Elements and Parton Showers in Hadronic Interactions*, JHEP **08** (2002) 015, arXiv: hep-ph/0205283 (cit. on p. 13).

[124] ATLAS Collaboration, *Measurement of $W^{\pm}$ and Z Boson Production Cross Sections in pp Collisions at $\sqrt{s}$ = 13 TeV with the ATLAS Detector*, ATLAS-CONF-2015-039, 2015, URL: https://cds.cern.ch/record/2045487 (cit. on p. 13).

[125] M. Aliev et al., *HATHOR: HAdronic Top and Heavy quarks crOss section calculatoR*, Comput. Phys. Commun. **182** (2011) 1034, arXiv: 1007.1327 [hep-ph] (cit. on p. 13).

[126] P. Kant et al., *HatHor for single top-quark production: Updated predictions and uncertainty estimates for single top-quark production in hadronic collisions*, Comput. Phys. Commun. **191** (2015) 74, arXiv: 1406.4403 [hep-ph] (cit. on p. 13).

[127] ATLAS Collaboration, *Measurements of $t\bar{t}$ differential cross-sections of highly boosted top quarks decaying to all-hadronic final states in pp collisions at $\sqrt{s} = 13$ TeV using the ATLAS detector*, Phys. Rev. D **98** (2018) 012003, arXiv: 1801.02052 [hep-ex] (cit. on p. 15).

[128] G. Bohm and G. Zech, *Introduction to Statistics and Data Analysis for Physicists; 2nd rev. ed.* Verlag Deutsches Elektronen-Synchrotron, 2014, ISBN: 978-3-935702-88-1, URL: http://bib-pubdb1.desy.de/record/169869 (cit. on p. 15).

[129] M. Czakon et al., *Top-quark charge asymmetry at the LHC and Tevatron through NNLO QCD and NLO EW*, Phys. Rev. D **98** (2018) 014003, arXiv: 1711.03945 [hep-ph] (cit. on pp. 20, 23).

[130] M. Czakon et al., *Top-pair production at the LHC through NNLO QCD and NLO EW*, JHEP **10** (2017) 186, arXiv: 1705.04105 [hep-ph] (cit. on p. 20).

[131] M. Czakon, D. Heymes and A. Mitov, *High-precision differential predictions for top-quark pairs at the LHC*, Phys. Rev. Lett. **116** (2016) 082003, arXiv: 1511.00549 [hep-ph] (cit. on p. 20).

[132] M. Czakon, P. Fiedler, D. Heymes and A. Mitov, *NNLO QCD predictions for fully-differential top-quark pair production at the Tevatron*, JHEP **05** (2016) 034, arXiv: 1601.05375 [hep-ph] (cit. on p. 20).

[133] URL: http://www.precision.hep.phy.cam.ac.uk/results/ (cit. on pp. 20, 21).

[134] M. Czakon, D. Heymes and A. Mitov, *Dynamical scales for multi-TeV top-pair production at the LHC*, JHEP **04** (2017) 071, arXiv: 1606.03350 [hep-ph] (cit. on p. 20).

[135] B. Grzadkowski, M. Iskrzynski, M. Misiak and J. Rosiek, *Dimension-Six Terms in the Standard Model Lagrangian*, JHEP **10** (2010) 085, arXiv: 1008.4884 [hep-ph] (cit. on p. 22).

[136] C. Zhang and S. Willenbrock, *Effective-Field-Theory Approach to Top-Quark Production and Decay*, Phys. Rev. D **83** (2011) 034006, arXiv: 1008.3869 [hep-ph] (cit. on p. 22).

[137] C. Degrande, J.-M. Gerard, C. Grojean, F. Maltoni and G. Servant, *Non-resonant New Physics in Top Pair Production at Hadron Colliders*, JHEP **03** (2011) 125, arXiv: 1010.6304 [hep-ph] (cit. on p. 22).

[138] D. Barducci et al., *Interpreting top-quark LHC measurements in the standard-model effective field theory*, (2018), ed. by J. A. Aguilar-Saavedra et al., arXiv: 1802.07237 [hep-ph] (cit. on p. 22).

[139] M. P. Rosello and M. Vos, *Constraints on four-fermion interactions from the $t\bar{t}$ charge asymmetry at hadron colliders*, Eur. Phys. J. C **76** (2016) 200, arXiv: 1512.07542 [hep-ex] (cit. on pp. 22, 23).

[140] K. Agashe et al., *LHC Signals for Warped Electroweak Neutral Gauge Bosons*, Phys. Rev. D **76** (2007) 115015, arXiv: 0709.0007 [hep-ph] (cit. on p. 22).

[141] B. Lillie, L. Randall and L.-T. Wang, *The Bulk RS KK-gluon at the LHC*, JHEP **09** (2007) 074, arXiv: hep-ph/0701166 [hep-ph] (cit. on p. 22).

[142] T. A. Aaltonen et al., *Combined Forward-Backward Asymmetry Measurements in Top-Antitop Quark Production at the Tevatron*, Phys. Rev. Lett. **120** (2018) 042001, arXiv: 1709.04894 [hep-ex] (cit. on p. 22).